Utrecht University

Generation of base data supporting a radiotherapeutic carbon dose engine using Monte Carlo methods.

Tom Niessen

Supervisors: T. Peitzmann

L. Glimelius

Department of Physics
Utrecht University

Abstract

Detailed calculations of the physical dose and relative biological effect (RBE) of ionising radiation are vital in radiotherapy. This is generally done by the dose engine of a treatment planning system (TPS), which relies on base data sets consisting of integrated depth dose distributions (IDDs) and differential particle spectra. In this study, the Monte Carlo (MC) transport and interaction code FLUKA has been used to generate a new, optimised set of base data in support of the RayStation carbon dose engine. Firstly, it has been identified that the new data is more consistent and less subject to statistical fluctuations. Secondly, significant changes in physical and RBE weighted dose between treatment plans generated with the old and new base data were found. Since the changes in RBE weighted dose could exceed clinical uncertainty limits, clinics may have to reconsider their dose prescriptions.

The new base data has been implemented in a development version of RayStation and may be released clinically in a future version. If so, the data will be used to calculate physical and RBE weighted dose in clinical applications.

Table of contents

List of figures

Chapter 1

Introduction

Radiotherapy is a type of cancer treatment where ionising radiation is used to target tumour tissue with the aim of killing malignant cells. Photon therapy has historically been the conventional treatment type. However, as a result of efforts made to limit the damage inflicted to normal tissue, an ever-important objective in radiotherapy, the application of particle beams is gaining momentum rapidly. The main rationale for the worldwide spread of especially proton and carbon irradiation methods is the favourable shape of the dose distribution of swift ions in matter and the relative increase of biological effectiveness towards the end of the range. Particle beams are characterised by an inverse depth dose profile, with low deposited dose in the entrance region followed by a dose maximum just before the end of the primary particle range (Bragg peak). This characteristic shape allows for very localisable dose delivery and dose conformation to extended volumes, even in large, deep-seated tumours. Additionally, healthy tissue can be spared sufficiently to greatly reduce chances of severe side-effects [12][16].

In clinical applications, a treatment planning system (TPS) is used by dosimetrists, doctors, clinicians and physicists to generate and optimise treatment plans. In order to calculate the dose distribution and biological effect of ionising radiation, various physics and radiobiological models are implemented in the dose algorithms of a TPS. The carbon dose engine of RayStation, the TPS developed by RaySearch Laboratories in Stockholm, Sweden, is mainly based on the pencil-beam dose algorithm and local effect model (LEM), which are used to calculate the physical dose distribution and biological effectiveness of carbon beams, respectively [1]. A primary requirement of these models is the presence of base data, consisting of:

  (i) Laterally integrated depth dose distributions (IDDs)

 (ii) Differential particle energy spectra of ion species with charge $Z \leq 6$

The base data sets are defined for mono-energetic carbon beams in water, which have been simulated with the Monte Carlo (MC) transport and interaction code FLUKA.

In this work, the aim is to review the current and create a new, optimised set of base data using the FLUKA MC code [13]. Particularly, the particle spectra will be enriched by inclusion of nitrogen ($Z = 7$) and oxygen ($Z = 8$). In order to evaluate the new data, comparisons between the old and new data will be performed under various circumstances. The comparative work can be classified into two categories:

(i) Comparisons of the pristine data. The IDDs and particle spectra will be compared with the aim of looking for differences in data quality, such as consistency and statistical fluctuations.

(ii) Comparisons of the delivered dose and biological effect in a set of treatment plans in RayStation. This will be done to assess changes in clinical cases caused by the implementation of the new base data.

Importantly, whereas the goal of the former is to evaluate and compare the quality of the data, the goal of the latter is merely to assess the effect of the data changes on treatment plans in clinical applications.

Chapter 2

Theory

2.1 Physical properties of particle beams

The next sections will describe important physical properties of particle beams and explain how these characteristics are exploited in ion radiotherapy. Furthermore, comparisons between photon, proton- and carbon-ion beams will be drawn to shed light on the rationale of particle therapy and to touch upon the reason for the evolution of radiotherapy towards particle beams. Importantly, since the average density of the human body is close that of water, a particle beam shows very similar characteristics in water and human tissue. Therefore, in everything reported in the following, beams traversing a water target will be considered, unless noted otherwise.

2.1.1 Dose distribution

In many cases the most natural and straightforward starting point of beam characterisation in radiotherapy is the study of energy loss by ionising radiation traversing through matter. Figure 2.1a displays a 2-dimensional histogram of the dose distributed by a simulated $400\,\mathrm{MeV/u}$ carbon beam in a water target. The particle beam starts off narrow in the entrance region and is subject to lateral spread due to multiple Coulomb scattering of the primary carbon ions as they traverse the target, before many particles come to a stop at around $37\,\mathrm{cm}$ depth. The peak region is followed by a dose tail[1]. The 2-dimensional dose distribution can be integrated laterally in order to obtain a so-called integrated depth dose distribution (IDD), also known as the Bragg Curve, which is shown in figure 2.1b for carbon-ion beams at five different energies. The curves display the characteristic inverse dose profile of particle beams in matter, with low entrance dose, referred to as the plateau, until the occurrence

---

[1] The origin of the dose tail, caused by light beam fragments, will be treated in later sections.

(a) 2-Dimensional dose distribution

(b) Integrated depth dose curves (IDD)
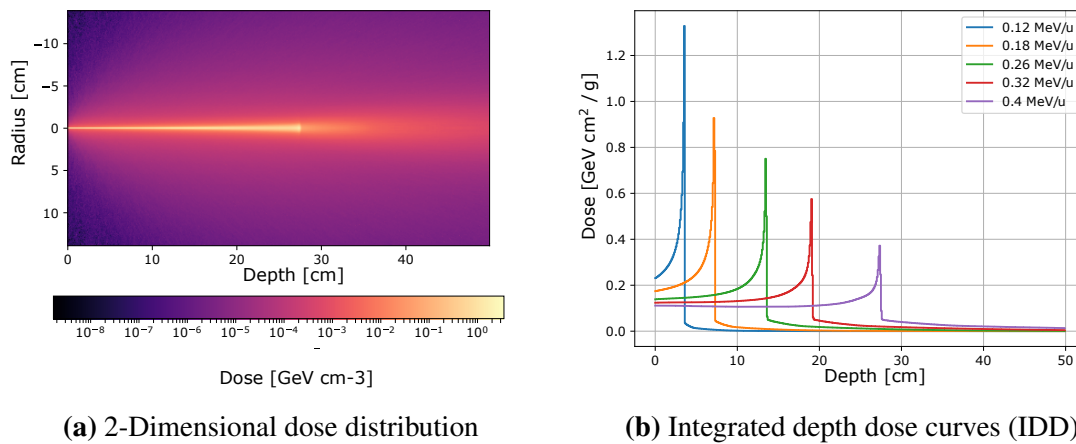
Fig. 2.1 a) Two dimensional histogram of the dose deposited by a $400\,\mathrm{MeV/u}$ carbon beam. b) Integrated depth dose distributions of carbon beams at five energies. Both plots were simulated in FLUKA for 5×10^5 particles.

of a sharply peaked dose maximum, known as the Bragg Peak, followed by a fragment tail. This characteristic shape exhibits what makes particle beams especially favourable for applications in radiotherapy, since the peaked dose-profile allows for precise localisation of the dose distributed. Especially when targeting deep-seated tumours, ion beams exploit their shape by sparing normal tissue in the entrance region and the region distal to the tumour while reaching elevated dose levels in the extended tumour volume.

Photon treatment has historically been the most used and accessible radio-therapeutic treatment method, and it still is. In most clinical cases, photon treatment is the main treatment method, whereas ion therapy serves as secondary treatment in cases where additional positive results can be achieved. Figure 2.2 displays the (relative) depth-dose distribution of photons, proton and carbon ions. The figure clearly shows the enhanced dose-profile of particle beams in comparison to photons. Additionally, dissimilarities between the carbon and proton dose profiles can also be observed. For example, the largely absent fragment tail in the proton beam and the increased sharpness of the carbon Bragg peak. These effects are comprehensibly due to the fact that protons and carbon ions are different particles that behave differently, leading to differences in lateral beam spread, range and dose levels. The most important beam characteristics and processes will be described in the following sections.

2.1.2   Spread out Bragg peak (SOBP)

In order to use particle beams to target a tumour, the beam has to be modulated to cover an extended target volume. Hence, the Bragg curve is spread out by using a superposition of
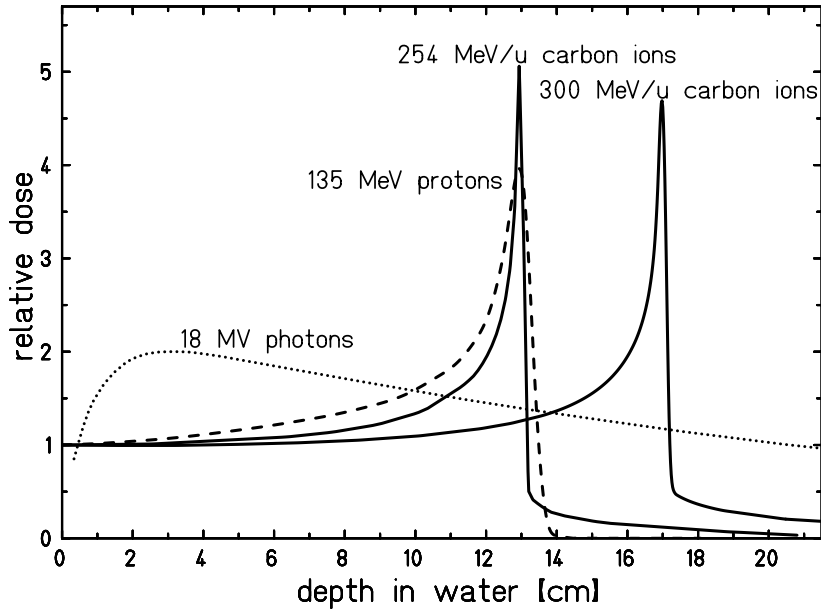
Fig. 2.2 Comparison of photon (dotted), carbon (solid) and proton (dashed) ion beam depth-dose distributions (Weyrather and Debus [16]).

many beams of different energies (and range) [16]. In addition to covering the full target volume an important requirement in radiotherapy is uniform dose coverage, which can be ensured by applying appropriate weighting to the individual Bragg peaks. An example of a *spread out Bragg peak* (SOBP) is shown in Figure 2.3, where proper weighting has been applied in order to uniformly target the tumour region.

The total physical dose deposited $D(z)$ at penetration-depth z in a SOBP can be calculated by multiplying the dose $d_i(z)$ of each individual Bragg peak i with the applied weight W_i:

$$D(z) = \sum_{i=1}^{n} W_i d_i(z), \tag{2.1}$$

where n is the number of energies the SOBP consists of [2].

2.1.2.1 SOBP delivery

In practice, layers of *spots* are placed inside the patient body, each of which is associated with a number of accelerated particles exiting the beam delivery system, targeted at the spot position. A spot can be characterised by its position, spatial width, nominal energy, and energy spread. Subsequently, each spot receives a weight corresponding to the desired number of carbon ions in the beam. The beam delivery system targets each distal layer of spots by controlling the nominal beam energy. Within each layer, magnets located perpendicular to
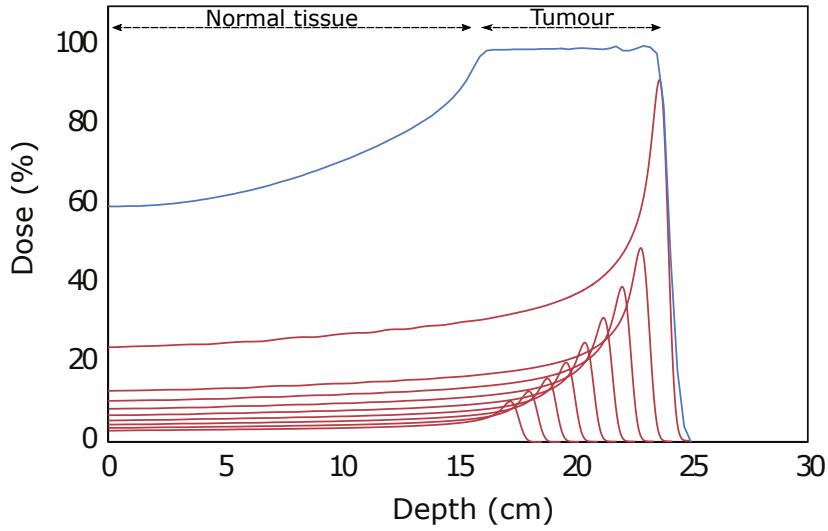
Fig. 2.3 Spread out Bragg peak (Grant and Chang [5]).

the beam direction deflect the beam in order to target every spot located in the layer. Figure 2.4 displays a visualisation of this state-of-the-art radiation technique, referred to as *active spot scanning* or *pencil beam scanning* .

2.1.3   LET and Bethe-Bloch

Before we can deal with other beam characteristics we require an overview of the underlying processes; a theoretical framework to understand energy loss and stopping power needs to be defined. Stopping power, or linear energy transfer (LET), is defined as the mean energy loss dE of a particle of energy E, per unit length traversed material dx: $\text{LET}(E) = \frac{dE}{dx}(E)$. For charged particles at low energies ($v \ll c$) the LET is mainly composed of two mechanisms, namely the *electronic* stopping power due to momentum transfer from the charged particles to the electrons in the surrounding medium and the *nuclear* stopping power due to elastic Coulomb scattering of the ions on the atoms in the traversed medium. A description of stopping power that incorporates the electronic stopping power, which is the dominant factor at radiotherapeutic energies, was formulated by Hans Bethe in 1930 and is called the Bethe formula [9]. The formula models the mean energy loss of charged particles traversing a medium due to interactions with target electrons. The non-relativistic version of the Bethe formula for a particle with velocity v and charge Z travelling through a target material with electron density N_e and mean excitation potential I reads:

$$-\frac{dE}{dx} = 2\pi \frac{e^4}{m_e(4\pi\varepsilon_0)^2} \cdot \frac{Z^2}{v^2} \cdot N_e \ln \frac{2m_e v^2}{I}, \tag{2.2}$$
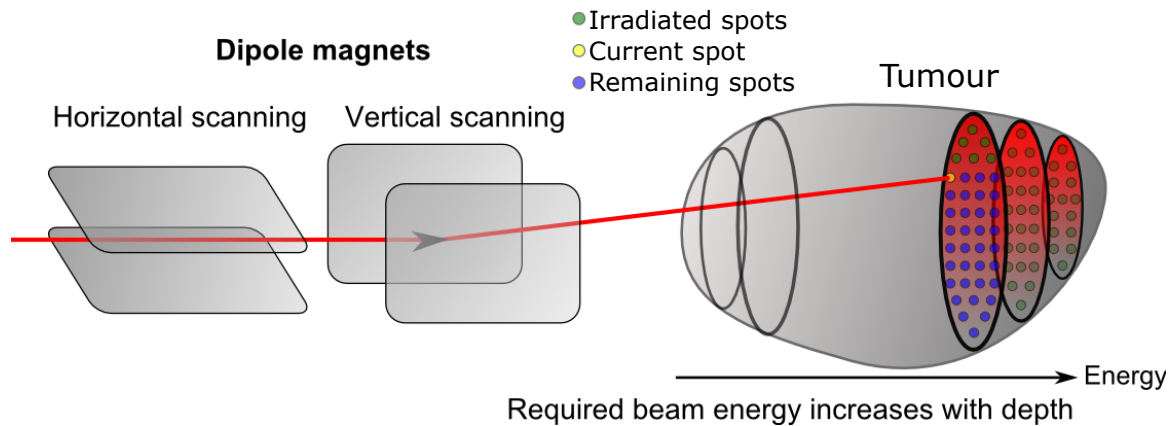
Fig. 2.4 Image of active spot scanning [19]. The particle beam is deflected by two sets of electromagnets in order to target each spot in the selected energy layer. The beam can target different energy layers by changing the beam energy.

where m_e, and e stand for the electron rest mass and charge, respectively, and ε_0 is the vacuum permittivity. Several corrections[2] have been omitted here, since they will have limited impact in clinical applications.

The mean excitation potential describes the target material and can be approximated by $I = 10(eV) \cdot Z$, with Z the atomic number of the target material's atoms. This was shown by Felix Bloch in 1933, the resulting equation is therefore generally referred to as the Bethe-Bloch equation [9].

The Bethe-Bloch equation reveals that at low energies the stopping power increases with $\sim 1/v^2$, intuitively explained by increased interaction times between particles and the surrounding electrons at lower velocities. This also explains why the particle dose distributions in figure 2.2 posses the characteristic peaked shape. As the ions lose energy, their stopping power increases, resulting in elevated dose deposition at the distal end of the particle range. Another important feature of Bethe-Bloch theory is that the stopping power of particles with the same velocity scales with Z^2/A. Hence, the range of particles increases with A/Z^2. This is why carbon beams need much higher energies than proton beams to achieve similar range. It also explains the so-called *fragment tail* we observe in carbon dose distributions, which we will talk about in the following section.

---

[2]Shell, Fermi's density, Barkas and Bloch corrections have been omitted (respectively of the order of Z, Z^2, Z^3 and Z^4)

2.1.4   Longitudinal range straggling

The range of a particle beam is largely dependent on the starting beam energy as shown in the Bethe-Bloch equation (eq. 2.2) and figure 2.1b. However, this does not mean that every primary particle in the beam loses energy in the same way. Due to the statistical nature of both energy depositions and deflections, ion beams do not stay mono-energetic as they traverse tissue, nor do all beam particles follow the same trajectory. Both these effects induce nonuniform particle range throughout the beam (i.e. varying penetration depths between the same initial and final energies), causing a more gradual dose buildup and falloff of the Bragg peak. The longitudinal widening of the Bragg peak is called *range straggling*. In order to define the range of a whole beam, the continuously slowing down approximation (CSDA) is used to calculate the mean energy loss per particle. Hence, one typically refers to the CSDA range.

The statistical nature of energy depositions, often referred to as *energy loss straggling*, causing both the number of energy loss events as well as the amount of energy lost in a single event are statistical in nature. Thus, two particles with the same starting energy that follow the exact same trajectory can have different kinetic energies throughout their paths, resulting in different ranges. Energy loss straggling is the dominant source of range straggling [12]. Analogously, due to the statistical nature of deflection events particle trajectories to a certain position do not have to be equal. This means that two particles travelling through a point can have different path lengths and thus, their energy can vary. This secondary source of range straggling is called *path-length straggling*. Both straggling effects can be observed in Figure 2.5.

As Bohr has shown, the range distribution $s(z)$ in a particle beam travelling through a medium in the z direction can be approximated by the following Gaussian distribution:

$$s(z) = \frac{1}{\sqrt{2\pi}\sigma_z}e^{-(z-R)^2/2\sigma_z^2},$$
(2.3)

where R is the nominal range (with $2 < R < 40$cm) [12]. The range-spread σ_z is inversely proportional to the square root of the particle mass number A [2], which explains why carbon beams are better localised than proton beams of similar range. This can be viewed in Figure 2.2.

2.1.5   Inelastic nuclear interactions (fragmentation)

Besides Coulomb scattering, heavy ions traversing tissue will undergo inelastic nuclear interactions in which the beam projectiles can lose one or more nucleons. The loss of primary
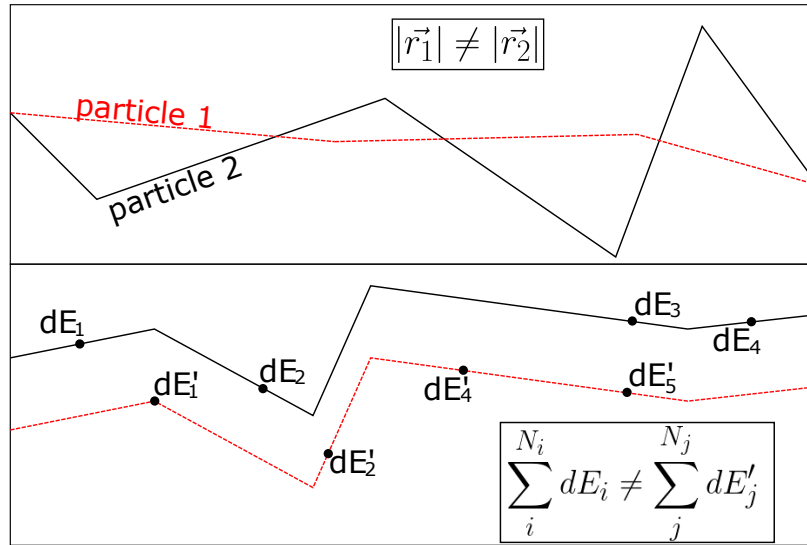
Fig. 2.5 Path-length straggling (top): two particles follow different trajectories between the same initial and final position. Energy-loss straggling (bottom): two particles following the same trajectory can undergo different energy-loss events. Both straggling effects result in different end-of-track energies.

ions resulting in buildup of secondary charged particles (with lower mass) is the phenomenon we call *fragmentation*. Figure 2.6b displays the buildup curves of all ion species with charge $Z \leq 6$ in a 400 MeV/u carbon ion beam in water. We see that attenuation of the primary ion flux[3] results in the buildup of lighter fragments. Consequently, the dose distributed will not solely consist of dose from primary ^{12}C, but significant fragment dose contributions will arise, especially at higher depths. Figure 2.6a shows how the buildup of fragment beam flux results in physical dose contributions in a 400 MeV/u carbon ion beam in water. The beam starts with just primary dose contribution in the entrance region, but as the primary carbon ions traverse the medium, some will undergo inelastic collisions resulting in fragment buildup and subsequent fragment dose contributions. After the Bragg peak region where all primary ^{12}C ions have come to a stop, we are left with residual fragment dose, also known as the *fragment tail*. The main cause of the fragment tail is the A/Z^2 range dependence we have seen above. Following nuclear interactions the newly formed fragments continue travelling with similar velocity and direction. Since particle range increases with A/Z^2, the fragment dose will consist of a variety of particle species and ranges, resulting in the fragment tail region. Note that in figure 2.6 we do not discriminate isotopes, due to the fact that LET, if expressed in MeV/u, does not differ between isotopes of the same ion species. For example,

---

[3]Flux is the rate of particles passing through a surface, in our case the section of the cylinder in which dose is measured.

(a) Fragment dose contribution
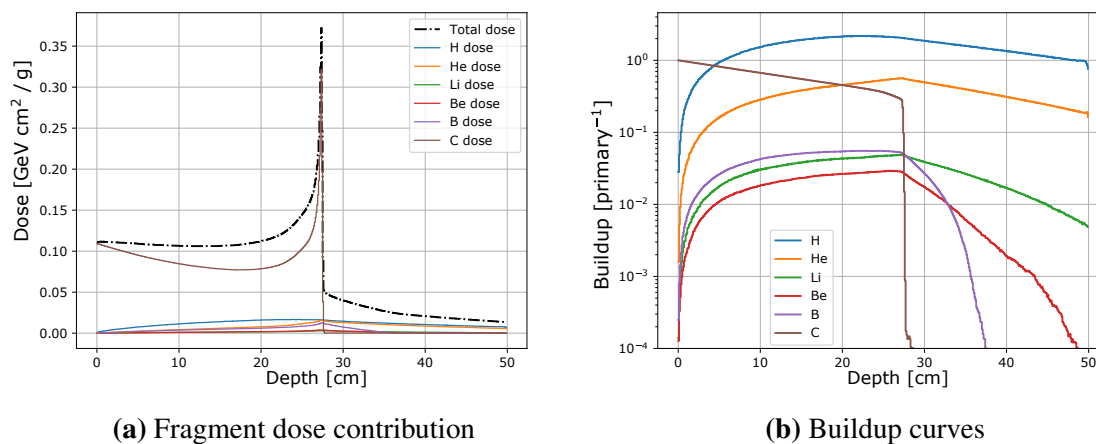
(b) Buildup curves

Fig. 2.6 Dose distributed (left) and buildup curves (right) of all ion species with $Z \leq 6$ inside a simulated 400 MeV/u carbon beam. No isotopic discrimination was made.

the carbon dose contribution contains dose due to both primary ^{12}C as well as fragment ^{11}C and ^{10}C ions.

The amount of fragment buildup in the beam is dependent on the probability for inelastic nuclear interactions, which can be influenced by several beam properties. First of all, fragment buildup increases with the range of the beam; the longer primary ions travel, the higher the chance of an inelastic collision. Thus, the relevance of fragmentation increases with beam energy. This can be observed in Figure 2.1b, showing that the height and length of the fragment tail increases with the beam energy. Secondly, the probability of inelastic collision is greatly influenced by the primary ion size. Larger ions have higher chance of inelastic collisions with target atoms, as well as a wider variety of fragment ion species emerging after such interactions. Consequently, this means that modelling of heavier ion beams, such as carbon, is more complex than proton beams, since all secondary fragments have to be modelled separately with different cross sections.

2.1.5.1 Target recoils

Besides the creation of smaller fragments, inelastic collisions between carbon ions and water molecules can result in the emittance of oxygen and nitrogen atoms[4]. These so-called target recoils will contribute to the dose profile and can even take part in inelastic collisions again. Therefore, oxygen and nitrogen will be included in further research reported here.

---

[4]In theory, there can be other, heavier, target recoils, but this is generally neglected.
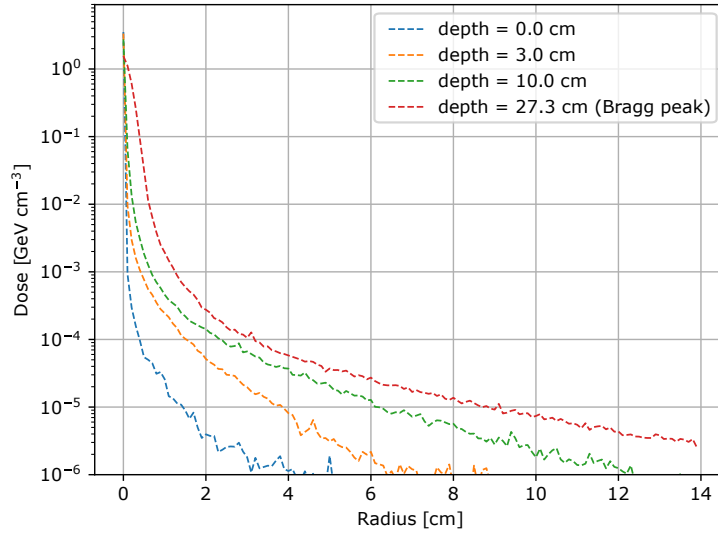
Fig. 2.7 Total distributed dose as a function of lateral position inside a 400 MeV/u carbon beam at 4 depths.

2.1.6 Lateral spread

As we have seen in 2.1a the carbon dose profile is subject to lateral widening with increasing penetration depth towards the Bragg peak. This can be observed closely in Figure 2.7, showing the lateral dose profile in a 400 MeV/u carbon beam at 4 different depths.

A cause of the beam broadening and lateral spread in the dose profile are the elastic collisions between primary beam particles and the target nuclei. Many of such small-angle deflections induce primary ions to diverge from the primary beam axis, an effect called Multiple Coulomb Scattering (MCS). The lateral distribution due to MCS can be modelled to first order by a Gaussian that transforms (but remains Gaussian) as the beam penetrates the tissue. The mean MCS angle $\bar{\theta}_0$ is then approximated by

$$\overline{\theta_0} \approx \frac{z \cdot 10.6 \text{MeV}}{E_k} \sqrt{\frac{1}{X_0}} \tag{2.4}$$

where we have primary ion charge z and kinetic energy E_k and the material property radiation length X_0. The inverse dependence of the scattering angle on the kinetic energy explains the widening of the beam near the Bragg peak region, where most primaries come to a stop. The radiation length varies with Avogadro's number A and the primary species' atomic number Z and weight A to the following relation: $X_0 \sim A/NZ(Z+1)$. This is the source of the increased widening of proton beams with respect to carbon beams of up to a factor of 3.5.

Firstly, because of the different charge-to-mass ratio of protons and secondly, because proton beams need less starting energy to achieve the same range (as we have seen in Equation 2.2).

Another effect contributing to the lateral beam spread are inelastic nuclear interactions that cause fragmentation in the beam, as seen in section 2.1.5. These secondary particles are modelled in the so-called *nuclear halo*, which includes all particles scattered at large angles, both from elastic and inelastic interactions. Hence, besides the secondary fragments, the nuclear halo includes target recoils and ejectiles from nuclear reactions, as well as the non-Gaussian part of MCS.

The total lateral beam spread can be seen as a combination of MCS and inelastic nuclear scattering, which can by modelled by a superposition of Gaussian distributions. Typically, one inner Gaussian is used to describe the small-angle, Gaussian part of MCS, where as the nuclear halo is described by a combination of one or more Gaussian distributions with different width [10].

2.2 Biological Effectiveness

Physical dose deposition profiles are not the end point of particle beam radiotherapy, since ultimately we are interested in the damage that has been inflicted to tissue, i.e. cell killing. In order to accurately compute inflicted damage, the quality and biological effectiveness of radiation have to be determined.

Figure 2.8 shows physical dose distributed (top panel, solid line) by a ^{12}C particle beam, the middle panel shows the resulting survival curve. It displays how the favourable shape of the physical dose profile supports the radiation of tumour tissue while sparing normal tissue. Additionally, elevated biological effectiveness in the SOBP further re-enforces tumour cell death.

2.2.1 RBE

It is standard practice in radiotherapy to compare biological effectiveness of the radiation type in question to a reference radiation type, referred to as *relative biological effectiveness* (RBE) [17]. It is defined as the ratio of delivered dose by both radiation types that lead to *equal biological effect*, i.e.

$$RBE = \frac{D_{ref}}{D_{particle}}\bigg|_{Iso\text{-}effect}, \tag{2.5}$$

where $D_{particle}$ and D_{ref} are the dose delivered by particle radiation and the reference type, respectively. RBE is an empirical quantity that can be defined in various ways as a function
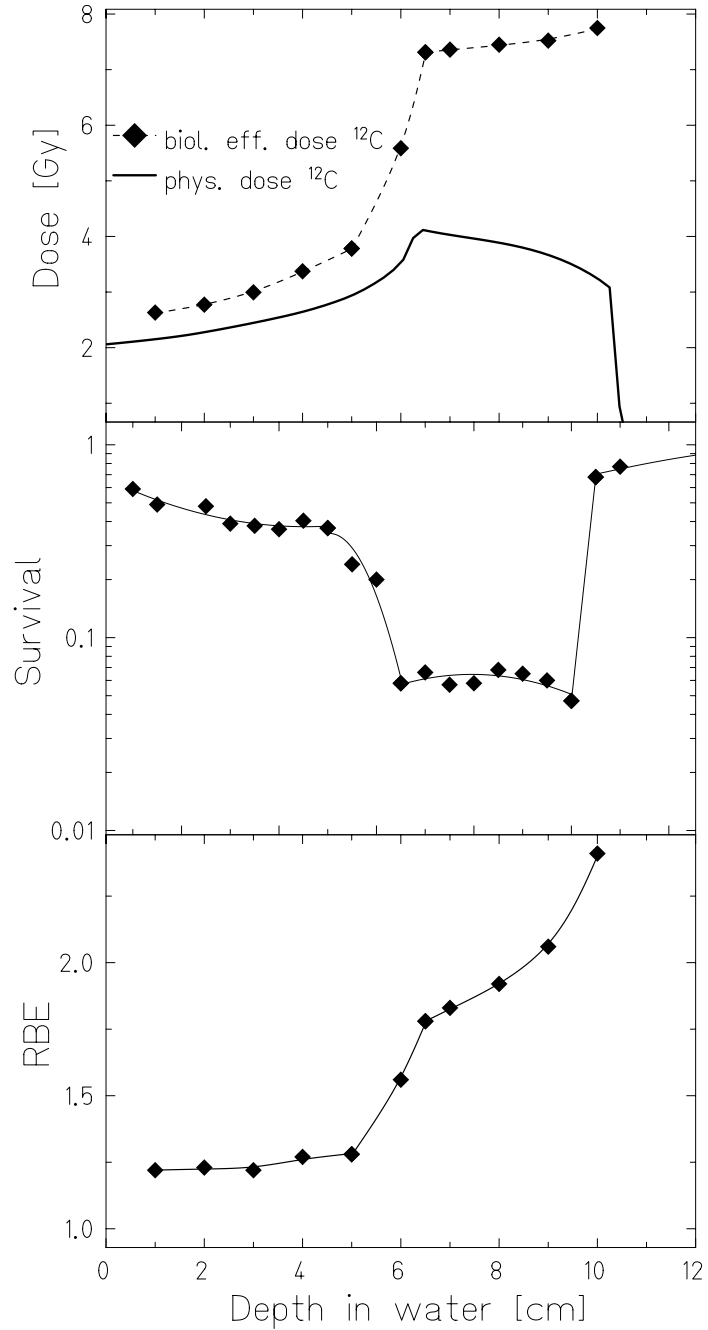
Fig. 2.8 Top: Physical dose and biological effective dose. Middle: Survival curve corresponding to the physical dose curve. Bottom: Computed RBE (Weyrather and Debus [16]).

on quantities that are deemed relevant. One can define RBE as a local property in tissue as a function of radiation type, cell type and/or other physical quantities, but RBE can also be defined as a function of depth in water. Historically, photon beams (X-ray) have been the most used radiation method in oncology; for a long time photon treatment was the core knowledge of dosimetrists and doctors and even still, radiotherapy prescriptions are described in terms of photon dose. Hence, when other types of ionising radiation emerged there was the desire to compare results to the traditional radiation methods. This lead to the standardisation of RBE as the quantity to express radiation quality with X-ray as the reference radiation type.

An example of how RBE can be calculated is displayed in figure 2.9, which shows the cell survival as a function of dose for three radiation types. The horizontal line indicates where all three radiation types achieve a cell survival probability of 0.1. The RBE values corresponding to this survival rate (using X-ray as the reference dose) are respectively 1.6 and 3.74 for the 266.4 MeV/u and 11.0 MeV/u carbon beam. There are many micro- and macroscopic factors influencing biological effectiveness of radiation [12][17], including, but not limited to:

- Type of radiation

- Linear energy transfer (stopping power)

- Properties of the irradiated cells

- Radiation energy

The choice of reference radiation type gives rise to additional ambiguity in the definition of RBE, as the choice of reference dose can not only change over time, it can even vary with geographical location. For example, in contrast to Europe and North America, where X-ray dose is universally used as the reference radiation type, Japanese clinics often use neutron radiation as the reference type (for historic reasons) [6]. Due to this divergence in RBE definitions it is not possible to simply perform RBE comparisons. To support comparisons and collaborations between these regions RBE values often have to be cross-computed between both RBE definitions.

2.2.1.1 Biological effective dose

After calculation of RBE, the corresponding physical dose curves can be weighted with the RBE distribution to create *RBE weighted dose*, also abbreviated as *Biological effective dose* or simply *RBE dose*. It is generally used as the primary measure of radiation quality as dosimetrists and clinicians often define clinical goals and requirements in terms of RBE dose.
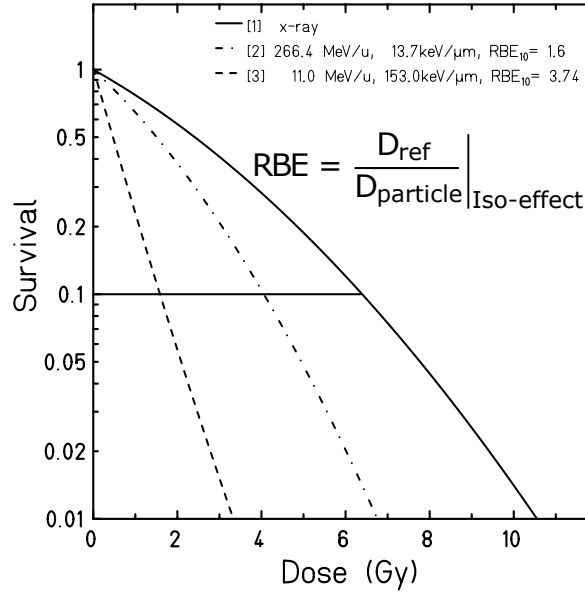
Fig. 2.9 Cell survival probability as a function of dose for three different radiation types: X-ray, carbon 11.0 MeV/u and carbon 266.4 MeV/u(Weyrather and Debus [16]).

The bottom panel of Figure 2.8 displays the RBE distribution corresponding to the physical dose and survival curves above in the panels above. RBE dose as a function of depth can now be defined as

$$\text{RBE dose}(z) = \text{Physical Dose}(z) \times \text{RBE}(z), \tag{2.6}$$

where physical dose is denoted in units of *Gray* (Gy) and RBE dose in units of GyRBE. The resulting biological effective dose curve can be observed in the top panel.

2.3 Carbon ion dose calculation in RayStation

Computation of physical dose, biological effect and the corresponding RBE weighted dose is complex matter where various physical models and approximations have to be implemented into a *treatment planning system* (TPS). A TPS is software that is used by dosimetrists, doctors, clinicians and researchers to perform geometric patient modelling and generate plans based on clinical requirements.

The TPS that will be used in this work is RayStation, developed by RaySearch Laboratories in Stockholm, Sweden. The next sections will provide a global description of the (physical) models that have been implemented in the RayStation carbon ion dose and RBE
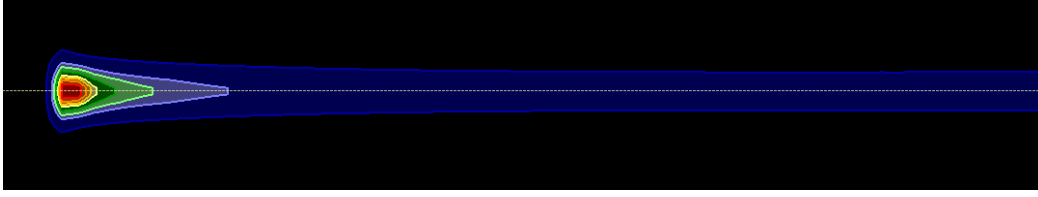
Fig. 2.10 Dose histogram of a carbon ion pencil beam.

weighted dose engine. Ultimately, we will work towards an explanation of the work done here in support of the dose engine.

2.3.1 Physics models

2.3.2 Pencil beam dose algorithm

In the RayStation dose engine the patient body is modelled in a 3-dimensional voxelised grid. Intersecting the grid, a collection of spots is placed inside the patient body. As explained earlier, each spot is associated with a number of accelerated particles exiting the beam delivery system, targeted at the spot position. The dose distribution of a single spot is determined using the so-called *infinite slab approximation* in which the patient geometry is treated as a composition of cylindrical slabs, unbounded in the radial direction. Because of this approach a spot will not capture effects due to lateral inhomogeneities. Consequently, the dose profile obtains radial symmetry that, together with the peaked depth dose distribution (*see section 2.1.1*), leads to a pencil-like shape. Therefore, the algorithm is referred to as the *pencil beam dose computation algorithm*. It is a standard and widely used algorithm, e.g. in Parodi et al. [13]. Figure 2.10 displays an example of a (carbon) pencil beam.

The dose deposited d_{pb} by a pencil beam in a voxel located at radiological (water-equivalent) depth z and lateral distance r with the beam axis is

$$d_{pb}(r,z) = \Phi(r,z)IDD(z) \tag{2.7}$$

where $\Phi(z,r)$ is the normalised lateral dose profile and $IDD(z)$ is the integrated depth dose distribution of the beam. Both dose profile components are obtained by scaling reference dose profiles in water to the target material by calculation of radiological depth distribution throughout the tissue. Subsequently, the total dose d delivered in a voxel is obtained with the weighted sum over all spots j in all energy layers e in all beams b in the beam set:

$$d(x,y,z) = \sum_b \sum_e \sum_j w_{bej} d_{bej}(x,y,z) \tag{2.8}$$

where w_{bej} is the weight of each spot.

2.3.2.1 Energy loss

The dose deposited in the patient at a certain depth z is determined by reference depth dose curves in water. In order to do this, first the water-equivalent depth z_{eq} needs to be calculated. This can be done by taking the ratio of the stopping power in water $\text{LET}_w(E(z))$ and in the medium $\text{LET}(E(z))$ and integrating over the path length, giving

$$z_{eq}(z) = \int_0^z \frac{\text{LET}(E(z'))}{\text{LET}_w(E(z'))} dz', \tag{2.9}$$

which is solved using the 4-point Runge-Kutta method. This means that absolute stopping power is not used to directly calculate the dose deposited by the ionising radiation, but rather for calculations of radiological depth, which is in turn used to sample deposited dose from reference integrated depth dose curves (IDDs).

The electronic stopping power is calculated by a form of the Bethe-Bloch formula [14], rewritten as

$$\text{LET} = a_1 \kappa \frac{\rho Z^2}{\beta^2} \left[a_2 - \ln\left(\frac{1}{\beta^2} - 1 \right) - \beta^2 \right]$$
$$\text{with } \beta^2 = 1 - \left(1 + \frac{E}{Mc^2} \right)^{-2} \text{ and } \kappa = \frac{4\pi e^4}{m_e c^2}, \tag{2.10}$$

where m_e, and e are the electron rest mass and charge, respectively. The beam dependent quantities are the kinetic energy E, atomic number Z and mass M of the carbon ions. Then, there are the following dependent quantities ρ, the density of the target material, a_1 and a_2. The latter two are given by

$$a_1 = \frac{1}{u} \sum_i w_i \frac{Z_i}{A_i} \text{ and} \tag{2.11}$$

$$a_2 = \ln \frac{2m_e c^2}{I}. \tag{2.12}$$

Equation 2.11 conveys the elemental composition of the target tissue by summing over all constituent atom species, where each species i has atomic weight Z_i, mass number A_i and relative occurrence w_i. Equation 2.12 holds the mean excitation energy I. In the latter equations u and c denote the atomic mass unit and speed of light, respectively.

2.3.2.2 Multiple Coulomb Scattering

Lateral spread of the carbon ion beam due to Multiple Coulomb Scattering (MCS) is handled by implementation of Fermi-Eyges transport theory, which models the propagation of incident Gaussian beams through homogeneous slabs of material [4]. The beam stays Gaussian in shape as it propagates and is characterised at depth z by the set of spatial-angular moments $\left\{\overline{\theta^2}, \overline{r\theta}, \overline{r^2}\right\}$, which denote the angular variance, spatial-angular covariance (beam divergence) and the spatial variance, respectively. Here, θ denotes the projected scattering angle and r is the lateral distance from the central beam axis.

Next to depending on z and each other, the distribution moments depend on the scattering power T. Scattering power T is the rate of change of the angular variance, i.e. $T \equiv \frac{d\langle \theta^2 \rangle}{dx}$, due to MCS with penetration depth z (not to confuse with the stopping power, which is the rate of change of the energy with penetration depth) [4]. It can be calculated with the Rossi formula:

$$T = \left(\frac{E_s}{p\beta c}\right)^2 \frac{1}{X_0} \tag{2.13}$$

where X_0 is the composite radiation length of the tissue and p is the momentum of the carbon ions. Analogous to equation 2.11, the composite radiation length is the weighted sum of the material's constituent radiation lengths. It is important to note that while the constant E_s was by given by Rossi as $E_s = 21\,\text{MeV}$, in practice a value of $18\,\text{MeV}$ was used to comply with studies on published measurements of lateral spread in water.

An important limitation of the treatment of MCS lateral spread done here comes from the fact that Fermi-Eyges theory does not model lateral inhomogeneities, since it defines uniform slabs of material. This could give rise to errors in the lateral dose spread when a beam's trajectory lies adjacent to a different kind of tissue (bone tissue for example). Secondly, Fermi-Eyges transport only considers an incident Gaussian beam that stays Gaussian while traversing material and therefore, it disregards non-Gaussian tails created by MCS. Additionally, a clinical beam escaping the nozzle might not be perfectly Gaussian.

2.3.2.3 Nuclear halo

Lateral beam spread in a carbon ion beam is divided in a narrow, Gaussian distribution due to small-angle scattering and a wider distribution around the beam axis. While the first one is associated with MCS, and thus mainly contains carbon ion dose, the latter is mainly associated with inelastic nuclear interactions leading to fragmentation of the beam into smaller fragments. This low-intensity part of the beam will be referred to as the *nuclear halo*. The nuclear halo in the RayStation dose computation is approximated with a *quadruple*

Gaussian, a superposition of four Gaussian distributions with different widths. Subsequently, it was found that these widths can be parametrised as a function of depth, resulting in the so-called nuclear halo parameters [8]. The dose engine uses these predefined parameters to model dose deposited as a superposition of beams at each depth.

2.4   The local effect model (LEM)

The next step after calculation of physical dose by the pencil beam dose algorithm is the computation of RBE and RBE weighted dose. The theoretical framework for these computations is provided by the Local Effect Model (LEM), which is built on three key axioms that allow for derivation of the biological effect of ion irradiation from photon survival curves. Importantly, photon survival curves are known from decades of pre-clinical research, supported by the introduction of the concept of local dose. The next sections will concisely explain the Local Effect Model, following the reasoning of the original LEM papers by Krämer and Scholz [10][11][15].

2.4.1   Axioms

The first version of the LEM was developed at GSI Helmholtzzentrum für Schwerionen-forschung in Darmstadt by Scholz and collegues [10] [15]. It is based on a few key axioms that connect locally deposited ion dose with biological effect:

1. Lethal events (events that lead to cell death) are caused by energy depositions in a sub-volume of the cell nucleus, leading to local damage in the DNA. These local energy deposition are referred to as *local dose*.

2. The biological effect of local dose is independent of the type of radiation, i.e. equal local dose leads to equal local effect, independent of the type of particle depositing the dose.

3. Local dose in photon radiation is homogeneous throughout the target. While photon dose may vary on a macroscopic scale, local dose is considered to be homogeneous. This means that local dose in photon radiation can be acquired by studying cell survival curves that have been obtained on a macroscopic scale.

The first axiom indicates that the calculation of biological effect in the patient body relies on the *microscopic* quantity local dose. This can be emphasised by the intuitive argument that it is in fact a microscopic effect that dictates biological effect, i.e. lethal interactions

with DNA causing cell death. Hence, it is not possible to derive the biological effect directly from *macroscopic* physical dose distributions and particle energy spectra. We are required to describe local dose deposited around single ion tracks in order to compute cell survival curves.

Connecting the second and third axioms, we can say that the biological effect from *ion* dose depositions can be derived from macroscopically obtained *photon* survival curves.

2.4.2 General formulation of LEM

The derivation of biological effect in particle beams starts from the description of cell survival probabilities in photon beams. Lethal events in tissue that is irradiated by photons are randomly distributed in the cell population. The cell survival probability S_X[5] can be considered to be distributed exponentially with mean N_X, the average number of lethal events, i.e.

$$S_X = e^{-N_X}. \tag{2.14}$$

Next, we can define the lethal event density v_X inside a cell with volume V_{nucleus} by

$$v_X(d) = \frac{N_X}{V_{\text{nucleus}}} = \frac{-\log S_X(d)}{V_{\text{nucleus}}} \tag{2.15}$$

where the local photon dose dependence d has been introduced by substitution of equation (2.14). Analogously, one can define the cell survival probability and lethal event density in ion radiation as

$$S_{\text{ion}} = e^{-N_{\text{ion}}}$$
$$v_X(d) = \frac{N_{\text{ion}}}{V_{\text{nucleus}}} = \frac{-\log S_{\text{ion}}(d)}{V_{\text{nucleus}}}. \tag{2.16}$$

According axiom 2 and 3 (from section 2.4.1) the average number of lethal events in ion radiation N_{ion} can now be calculated by integrating the lethal event density $v_X\big(d(x,y,z)\big)$ over the cell nucleus, with the introduction of the *in-homogeneous* local ion dose $d(x,y,z)$:

$$N_{\text{ion}} = \int v_X\big(d(x,y,z)\big)dV. \tag{2.17}$$

Subsequently, equations (2.15) and (2.16) can be substituted in order to obtain the following expression:

$$-\log S_{\text{ion}} = \int \frac{-\log S_X\big(d(x,y,z)\big)}{V_{\text{nucleus}}}dV, \tag{2.18}$$

---

[5]Quantities describing photon radiation will be denoted by the subscript X.

which comprises the essence of the LEM. In order to solve equation (2.18) in clinical treatment cases, sufficient descriptions of photon cell survival $S_X(d)$ and the distribution of local ion dose $d(x,y,z)$ are required. These will be given in the following sections.

2.4.3   Photon cell survival curves

Historically, describing cell survival after photon irradiation has been an important objective in pre-clinical research. A parameterisation that has shown well agreement with experimental data is the linear-quadratic model for doses lower than threshold dose D_t with an exponential fall-off for doses greater than D_t. The resulting parameterisation is

$$-\log S_X(d) = \begin{cases} \alpha d + \beta d^2, & \text{if } d \leq D_t \\ \alpha D_t + \beta D_t^2 + s_{\max}(d - D_t), & \text{if } d \geq D_t \end{cases} \tag{2.19}$$

where the maximum slope is denoted by $s_{\max} = \alpha + 2\beta D_t$.

The parameterisation in equation (2.19) is valid for any modality and cell type by appropriate choice of values of $\alpha [Gy^{-1}]$, $\beta [Gy^{-2}]$ and $D_t [Gy]$. For example, the parameter values for photon irradiation were determined experimentally from survival curves (figure 2.8) as $\alpha_X = 0.1\,\mathrm{Gy}^{-1}$, $\beta_X = 0.05\,\mathrm{Gy}^{-2}$ and $D_{t,X} = 30\,\mathrm{Gy}$. Later, we will see how both photon and particle cell survival are required in order to compute RBE dose for particle radiation.

2.4.4   Distribution of local dose

Local dose $d(r)$ is regarded as the radial distribution of dose around a charged particle track. Here, local dose is described corresponding to the original LEM papers (LEM-I). However, in later research alternative descriptions of local dose have been proposed, and it is still a topic of discussion.

Outside of the maximum radius $r_{\max}$ the dose distributed is assumed to be zero. Inside $r_{\max}$ the dose is inversely proportional to r^2, achieving its maximum value at the track core radius r_c, below which the dose is approximated as constant. The resulting local dose relation is given by

$$d(r) = \begin{cases} \frac{\lambda \cdot \frac{dE}{dx}}{r_c^2}, & r < r_c \\ \frac{\lambda \cdot \frac{dE}{dx}}{r^2}, & r_c \leq r \leq r_{\max} \\ 0, & r > r_{\max} \end{cases} \tag{2.20}$$

where $\frac{dE}{dx}$ is the particle's LET and λ is a normalisation constant to ensure that integrating equation (2.20) over space returns the unrestricted LET[6], given by $\lambda = 1/(2\pi \cdot (\ln \frac{r_{\max}}{r_c} + \frac{1}{2}))$, where C is a unit conversion factor.

The leading particle properties that determine the form of the local dose distribution as well as the total dose deposited in a particle track are the particle's charge (Z) and kinetic energy, since they directly affect LET, r_c and $r_{\max}$.

2.5 Carbon RBE calculation in RayStation

The survival relations as derived in the last section can be used to calculate RBE and RBE dose in clinical cases by means of two algorithms that have been implemented into RayStation: the 'classic' algorithm and the low-dose approximation.

Vital in both algorithms is the definition of RBE weighted dose: the photon dose that would have to be delivered to reach the same biological effect as the physical ion dose, the latter of which is calculated by the pencil beam dose algorithm as described in section 2.3.2. Hence, RBE dose can be obtained by solving equation (2.19) for dose, which will now be denoted by D_{RBE}, resulting in

$$D_{RBE}(\vec{r}) = \begin{cases} \sqrt{-\ln S(\vec{r})/\beta_X + (\alpha_X/2\beta_X)^2} - (\alpha_X/2\beta_X), & -\ln S(\vec{r}) \le -\ln S_{\mathrm{cut}} \\ (-\ln S(\vec{r}) + \ln S_{\mathrm{cut}})/s_{\max} + D_{\mathrm{cut}}, & -\ln S(\vec{r}) > -\ln S_{\mathrm{cut}} \end{cases} \quad (2.21)$$

where the only unknown is $-\ln S(\vec{r})$, the biological effect of ion radiation throughout the patient (specific to each clinical case). All other terms are known constants.

2.5.1 Differential energy spectra

In order to calculate the biological effect $-\ln S(\vec{r})$ the algorithms require information about the distribution of particles throughout the patient body. As described in sections 2.1.3 and 2.1.5, attenuation of the primary beam flux results in the buildup of lighter (and few heavier) fragments due to inelastic nuclear interactions, leading to a so-called mixed radiation field. Each ion species has a distinct stopping power curve and thus, in order to calculate the biological effect contribution of each ion species present inside the beam, it is required to describe the phase-space of particles at each point in the radiation field. In RayStation, this is done

---

[6]The term *unrestricted stopping power* refers to the total energy released per unit length when integrating to infinite radius around the track.

on the basis of pre-stored differential energy spectra[7] that contain the energy distribution of each relevant ion species as a function of depth in water for various beam energies, measured in terms of *particles per primary per energy per area* $[(\text{primary})^{-1}(MeV/u)^{-1}cm^{-2}]$. An example of the energy spectra of a $450\,\text{MeV}/\text{u}$ carbon beam at three depths can be found in figure 4.2. A differential spectrum value is denoted by

$$\frac{dF}{dE}(E_{\text{beam}}, z, T, E), \tag{2.22}$$

the number of particles of type T and kinetic energy E at water-equivalent depth z for a beam with starting energy E_{beam}.

2.5.1.1 Fluence

An important quantity in the definition of differential particle spectra is fluence. It is defined by the number of particles travelling through a surface divided by the area of the surface in units of $[cm^{-2}]$. It can also be seen as the time integral of the flux density, which is the rate of particles per unit area.

2.5.1.2 Initial slope of the cell survival

In addition to differential energy spectra, the initial slope of the cell survival $\alpha_Z(T,E)$ (eq. (2.19)) is calculated for all particle species T and energies E in favour of computational efficiency with

$$\alpha_Z(T,E) = \frac{-\ln S_{\text{ion}}}{\overline{D}}, \tag{2.23}$$

ion where $-\ln S_{\text{ion}}$ and $\overline{D}$ are the biological effect and dose due to a particle traversal, respectively. Additionally, the initial $\beta_Z(T,E)$ can be calculated from (2.19).

2.5.2 The classic algorithm

In the classic algorithm, which is used for clinical dose computations, the biological effect $\ln S(\vec{r})$ is calculated as described in by Kramer and Scholz [10]. The following steps are performed to compute the RBE in each voxel:

1. Determine the voxel-specific particle energy spectra using the voxel's water-equivalent depth z_{eq} and equation (2.22). This will serve as the theoretical particle phase space inside the voxel.

---

[7]The term differential energy spectra is often abbreviated to *energy spectra*, *particle spectra* or *differential particle spectra*.

2. The total particle fluence F in the voxel centre can be calculated by integrating the energy spectra over the particle energy E and summing over all particle types T:

$$F = \sum_{t \in T} \int \frac{dF(z_{\text{eq}}, t, E)}{dE} dE, \tag{2.24}$$

which is then used to calculate the average number of 'hits' per cell nucleus as

$$\overline{N}_{\text{hit}} = F \cdot A_{\text{nucleus}}, \tag{2.25}$$

where A_{nucleus} is the area of a cell nucleus.

3. The actual number of hits N_{hit} is obtained by sampling from a Poisson distribution with mean $\overline{N}_{\text{hit}}$. This is done to account for the statistical nature of interactions between beam particles and the tissue.

4. The particles responsible for the hits are sampled from the theoretical particle phase space by sampling N_{hit} particles from the energy spectra (step 1). The result is an ensemble of $n = N_{\text{hit}}$ particles of type t and kinetic energy E: $\{t_i, E_i; k = 1, 2, \ldots, n\}$.

5. The absorbed dose by each hit D_{abs}^i is recursively accumulated in order to obtain the total dose

$$D_{\text{abs}}^i = c \cdot \frac{dE}{dx}(t_i, E_i) + D_{\text{abs}}^{i-1} \qquad i = 1, \ldots, n \tag{2.26}$$

where $D_{\text{abs}}^n = D_{\text{abs}}$ is the total absorbed dose in the voxel and c is a constant to convert the stopping power $\frac{dE}{dx}(T, E)$ to dose.

Analogously, the biological effect $-\ln S^i$ of each hit is accumulated using equation (2.19) as

$$-\ln S^i = c \cdot s(t_i, E_i) \frac{dE}{dx}(t_i, E_i) - \ln S^{i-1} \qquad i = 1, \ldots, n \tag{2.27}$$

where $s(T, E)$ is the slope of the survival curve, obtained from equation (2.14). Importantly, the slope of the survival curve of particle i depends not only on the particle type and energy (t_i, E_i), but also on previously absorbed dose, given by D_{abs}^{i-1} in equation 2.26.

Importantly, steps 3-5 are typically repeated a number of times (e.g. 1000) and the final dose computed from the average accumulated damage.

After calculation of the absorbed dose and biological effect inside the voxel, the RBE dose D_{RBE} is obtained by solving equation (2.21). The RBE factor is simply calculated using

$$\text{RBE} = \frac{D_{\text{RBE}}}{D_{\text{abs}}}. \tag{2.28}$$

Lastly, the final RBE weighted dose is calculated by multiplying the RBE factor with the physical dose calculated in the pencil-beam dose algorithm (see section 2.3.2). Note that this means that the doses calculated by the RBE dose algorithm are used solely to compute the RBE factor in each voxel, whereas, the physical dose is calculated in the pencil-beam dose engine.

2.5.3 The low-dose approximation

The sampling procedure in the classic algorithm can be very time consuming. Therefore, the low dose approximation [11] has been implemented into RayStation in support of the optimisation dose engine. The algorithm reasons that at low doses the number of particle transfers through a cell is so small that a 1-hit probability can be assumed. The cell survival probability due to the hit is obtained by computing an *average* particle from the particle phase space in the voxel. The procedure starts with calculating the initial slope of the survival curve due to a single particle traversal $\alpha_D(T,E)$, also called the *macroscopic* initial slope. It is calculated with

$$\alpha_D(T,E) = \frac{1 - \exp^{-\alpha_Z(T,E)d_1(T,E)}}{d_1(T,E)} \tag{2.29}$$

where d_1 is the dose deposited by one particle traversal through a cell, i.e.

$$d_1(T,E) = C \cdot \frac{dE}{dx}(T,E)/A_{\text{nucleus}}. \tag{2.30}$$

The β_D corresponding to α_D is calculated by scaling

$$\beta_D(T,E) = \left(\frac{\alpha_D(T,E)}{\alpha_Z(T,E)}\right)^2 \beta_Z(T,E) \tag{2.31}$$

Using the relations for the macroscopic LEM parameters (2.29) and (2.31), the average macroscopic LEM parameters in the voxel $\overline{\alpha}_D$ and $\overline{\beta}_D$ can be calculated by taking the

dose-weighted averages:

$$\overline{\alpha_D} = \frac{\sum_{T,E} \alpha_D(T,E) \cdot D(T,E)}{\sum_{T,E} D(T,E)}$$
$$\overline{\sqrt{\beta_D}} = \frac{\sum_{T,E} \sqrt{\beta_D}(T,E) \cdot D(T,E)}{\sum_{T,E} D(T,E)} \tag{2.32}$$

where $D(T,E)$ is the contribution to the total dose in the voxel from a particle of type T and energy E, obtained by weighting the stopping power with the particle fluence $\frac{dF}{dE}(E_{\text{beam}}, z, T, E)$.

Finally, the resulting average macroscopic LEM parameters can be used with equation 2.14 in order to calculate the (macroscopic) biological effect inside the voxel. Analogous to the classic algorithm, the RBE factor is then calculated by dividing the RBE weighted dose from equation (2.21) by the total physical dose, i.e.

$$RBE = \frac{D_{\text{RBE}}}{\sum_{T,E} D(T,E)}. \tag{2.33}$$

Lastly, the final RBE weighted dose is calculated by multiplying the RBE factor with the physical dose calculated in the pencil-beam dose algorithm (see section 2.3.2).

2.6   RayStation base data

As we have seen in earlier sections, the RayStation algorithms need various sets of pre-generated input data in order to compute physical dose and RBE weighted dose in clinical cases. In practice, clinics can choose to use the native RayStation base data sets or provide their own. The required base data consists of:

- IDDs for carbon beams in water in support of the pencil beam algorithm (section 2.3.2).

- Differential energy spectra of primary carbon ions and fragments (particle energy spectra) (section 2.5.1).

- Nuclear halo parameters (section 2.3.2.3).

- LET tables (sections 2.5.2 and 2.5.3).

- Initial cell survival slopes (section 2.5.1.2).

Here, we will focus on the IDDs and differential energy spectra currently present in RayStation in order to revise and optimise them with the goal of updating the clinically used data sets.

2.6.1 Integrated depth dose profiles

The current base data of RayStation for carbon consists of 896 mono-energetic IDDs with beam energies ranging between 50 MeV/u and 450 MeV/u. The beam energy interval of the IDDs was chosen such that the axial distance between two consecutive Bragg peaks is a maximum of 0.5 mm. To prevent extremely sharply peaked dose profiles an initial momentum spread of 1% was introduced. The IDDs were simulated in FLUKA in a water-filled cylindrical geometry of length 100 cm and radius 20 cm. The FLUKA built-in scoring method *USRBIN* was used to output laterally integrated dose with a depth bin resolution of 0.01 cm.

2.6.2 Particle energy spectra

The current particle energy spectra were simulated in FLUKA for 81 beam energies ranging between 50 MeV/u and 450 MeV/u. Analogous to the base IDDs, an initial momentum spread of 1% was introduced. The target is water-filled cylindrical geometry of length 50 cm and radius 5 cm with a depth bin resolution of 0.1 cm. The built-in scoring card *USRTRACK* was set to output the particle spectra as a function of particle energy for all isotopes with charge $Z \leq 6$. The kinetic energy of the primary particles ($Z = 6$) was binned linearly with $0 \leq E \leq 550$ MeV/u and a bin size of 1 MeV/u. For the fragments ($Z = 1 - 5$) logarithmic energy binning was applied, using 133 bins between 1 and 999 MeV/u. The lower limit of the energy binning chosen in accordance with results from other work (Elsässer et al. [3]).

Figure 2.11 displays an example of the energy spectra present in RayStation for a 300 MeV/u particle beam at 2 depths.
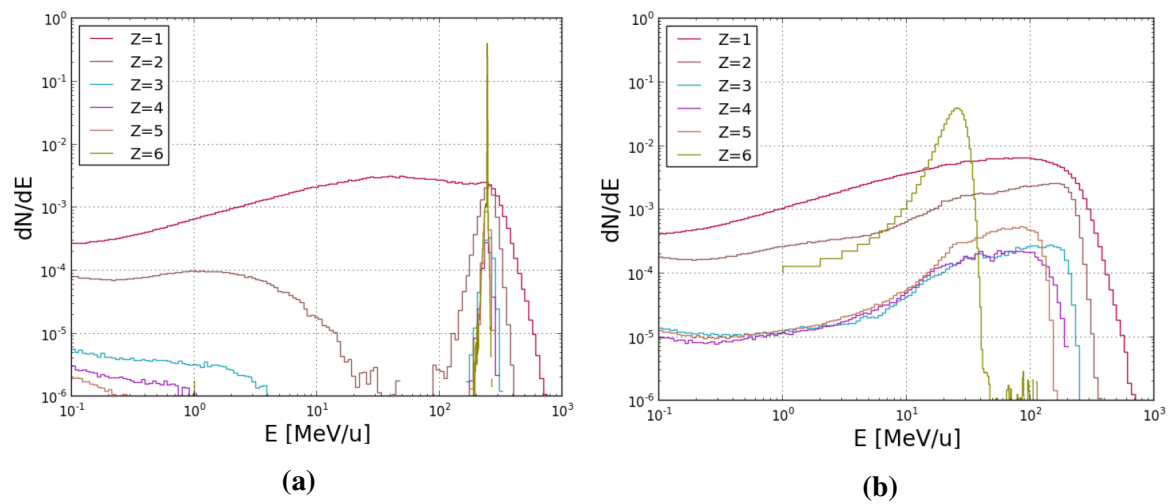
Fig. 2.11 Differential particle spectra in RayStation for a 300 MeV/u carbon beam at depth of (a) 5 cm (plateau region) and (b) 17 cm (Bragg peak).

Chapter 3

Methods

3.1   Data production in FLUKA

Since the start-up of particle therapy implementations in RayStation, the Monte Carlo (MC) engine FLUKA has been used for multiple applications such as base data generation. Therefore, the FLUKA MC code has here been chosen to simulate the transport and interaction of carbon ion beams in water in order to generate a complete set of base data for the RayStation dose engines.

FLUKA simulations are initiated with input files containing declarations of the system geometry, including the target materials, a beam and one or more detectors in the form of *scoring cards*. There is a library of scoring cards that can be used to output physical quantities such as dose and fluence. Another essentiality is an appropriate choice of the various transport and interaction settings available in FLUKA.

In all simulations reported here, the recommended default setting *hadrotherapy*, specifically tailored for particle beam therapy applications, was enabled. In addition, heavy ion nuclear interactions were activated. These settings ensure thorough transport of the primary beam particles and fragments and reliable handling of nuclear processes. The most important properties of these settings include:

- Creation and transport of electrons, positrons and photons (*EMF on*).

- The most accurate handling of charged particle Coulomb scattering (using inelastic form factor corrections).

- Maximum kinetic energy lost per step is set to 5% for all charged hadrons.

- Detailed transport of fragments and nuclear recoils (including multiple Coulomb scattering and nuclear interactions).

- Low-energy neutrons are transported down to thermal energies.

- The energy threshold below which hadrons lose all their energy instantaneously is set to 100 keV.

In the following sections the general physical, transport and geometrical settings of the IDD and energy spectra simulations will be described.

3.1.1   IDD simulations

Next to the settings reported above, some overwrites and additional settings were introduced in order to meet specific requirements in the IDD simulations. Firstly, the maximum kinetic energy loss per transport step has been overwritten to 2% (setting *FLUKAFIX*) in order to prevent a delayed buildup of electrons in the entrance region, which would cause a decreased dose deposition in the first few millimetres of the geometry. Secondly, it was found that statistics were improved by turning off the production of δ-rays (setting *DELTARAY*). Consequently, all energy transfers are assumed to take place as continuous energy losses. Lastly, an additional gain in statistics was obtained by limiting the maximum step size per transport step to 15 mm (setting *STEPSIZE*).

The beam energy range was chosen between 50 MeV/u and 500 MeV/u. The beam energy spacing between each consecutive simulation was chosen such that the axial distance between the Bragg peaks was approximately 0.5 mm in order to obtain spatially homogeneous coverage of Bragg peaks in the energy domain. In addition, to each beam an initial rectangular energy spread was introduced to ensure continuous coverage of every energy value between 50 and 500 MeV/u. This resulted in a total of 1097 semi mono-energetic dose profiles.

The system geometry was chosen sufficiently large to account for lateral beam spread and the dose tail, resulting in a 100 cm long cylinder of radius 35 cm. The dose deposited inside the cylinder was scored using the FLUKA built-in scoring card *USRBIN*, which detects the deposition of energy in GeV/g[1]. The spatial bin sizes of the binning structure were set to $(dr, dz) = (0.1, 0.01)$ cm, where r and z denote the radial and longitudinal coordinate, respectively. The final integrated depth dose profiles can be obtained by integrating over the lateral component. While in practice the integration limit can be chosen in accordance with the clinic's machine, here, we will retain the maximum limit of 35 cm. The simulations consisted of 10^6 primaries, which is sufficiently high to reach desired statistics.

---

[1]Gy can be obtained by multiplying GeV/g by $1.602176462 \times 10^{-7}$

3.1.1.1   Comparison to the previous IDDs

There are some key differences between the old IDDs and the new base data reported here. Firstly, in the new simulations electrons and positrons were created and transported, changing the handling of nuclear interactions. Secondly, changes were made in pursuit of better statistics: the maximum kinetic energy loss and step length in each MC transport step. Thirdly, the beam energy domain was expanded to include beam energies between 450 and 500 MeV/u, increasing the number of IDDs from 896 to 1097. It is also important to note that the simulations reported here were performed using a newer version of FLUKA (2011.2x.6) than in previous work. Since then, some new physics and transport methods have been introduced, which could have an effect on the results.

3.1.2   Energy spectra simulations

In contrast to the IDD simulations, where we are just interested in dose depositions, the goal of the spectra simulations is to obtain the energy distribution of each ion species as a function of depth, which requires very detailed handling of the transport and energy loss of the primary and secondary particles. For this purpose, the production of δ-rays was enabled above the kinetic energy threshold of 100 keV, which greatly decreases computational speeds. To compromise between computational speed and performance, the maximum kinetic energy loss was kept at the default value (5%). Apart from this, the energy spectra were run with the same transport settings as the IDDs.

   As an additional measure to limit computation times, the energy spectra are only simulated for every 20th energy of the IDD simulations, resulting in 55 simulated energies[2]. For the same reasons, the cylindrical geometry was limited to a depth of 50 cm. This could be done because for higher depths the RBE dose is very low and thereby, clinical cases with treatment depths that high are very rare. The radius of the cylinder was set to 35 cm to account for the lateral beam spread. The beam energy spread was chosen equal to the IDDs.

3.1.2.1   mgdraw

The old particle spectra were created using FLUKA's native scoring card USRTRACK, which was set to detect the differential particle energy spectra for each particle species. However, this functionality requires the definition of a high amount of small volumes in the geometry which is generally avoided in FLUKA. For this reason, rather than using a FLUKA native scoring card, an adjusted version of the user routine *mgdraw* was used to output a collision

---

[2]The energy spectra that have been omitted with respect to the IDDs are approximated in RayStation by interpolation of the existing spectra.

file. A collision file contains the relevant phase space of each energy loss event of each particle transported in the simulation. With that, it is possible to obtain the trajectory of each particle as well as the energy progress throughout the trajectories, which is then used to compute the differential particle spectra.

The total size of the collision files resulting from all 81 simulations is of the order of several terabytes. The methods used to parse and process the collision tapes will be described in later sections.

3.1.2.2 Comparison to the previous spectra

The most relevant difference between the new energy spectra generated here and the old RayStation spectra is the use of collision files output with mgdraw. While the USRTRACK method is easy to use and fast due to underlying optimisations, the mgdraw method yields extremely detailed information and allows for extensive research into the definition of energy spectra. Another notable difference is the inclusion of target recoils, oxygen and nitrogen ($Z = 7, 8$ resp.), in the spectra. This could affect both the physical and RBE dose. Lastly, the radius of the cylindrical geometry was changed from 5 to 35 cm, causing an increased fluence of low-mass and -energy fragments, which are the main fluence contributors in the outside region of the cylinder.

3.2   Data processing and visualisations in python

In order to parse, process and visualise the simulation data, a series of python scripts was developed. The scripts provide a platform in which the FLUKA output data (from USRBIN, USRTRACK and mgdraw) can be parsed and processed into data structures in which all data belonging to a set of simulations[3] can be stored. The platform was supplemented with a GUI that was used to visualise data output in support of data evaluations and comparisons. In addition, methods to transform the data to RayStation format were implemented. The next sections will describe the relevant data structures and functionalities of the code platform.

3.2.1   Dose profiles

Processing and storage of the dose profiles was very straightforward since the FLUKA output from USRBIN is already stored in the desired binning structure. In order to obtain IDDs, the dose profiles can be integrated laterally with integration limits set by the user. It is also

---

[3]A set of simulations indicates a group of identical simulations with different beam energies and energy spread.

possible to obtain the lateral dose profile (absorbed dose as a function of lateral distance) for any depth set chosen by the user.

3.2.2   Energy spectra

The generation of the energy spectra was computationally challenging, since very large binary collision files from mgdraw (section 3.1.2.1) had to be parsed and processed into a two dimensional binning structures (one positional and one particle energy component). In each spatial bin, the average differential energy spectrum of each ion species is stored in histograms.

Some additional functionalities in support of data post-processing and validation were implemented into the scripts. This included methods to compute spectra dose, particle buildup curves (figure 2.6b) and the spectra dose contribution of each ion species (figure 2.6a).

The energy binning of the differential energy spectra was chosen equal to previous spectra in RayStation, as reported in section 2.6.2. The newly introduced fragments O and N were binned in the same way as the other fragments.

3.2.2.1   Spectra dose

In this work, the statistical quality and consistency of the energy spectra is mainly evaluated by comparing the so-called *spectra dose* to the IDDs from USRBIN. The spectra dose is the dose distribution calculated from the energy spectra using the stopping power relations by summation of the energy spectra $\frac{dF}{dN}$ over all ion species Z and energies E. The spectra dose D_s at depth x is then given by

$$D_s(x) = N \sum_E \sum_Z \frac{dE}{dx}(E,Z)\frac{dF}{dN}(E,Z,x),\qquad(3.1)$$

where N is the number of primaries in the beam.

3.2.2.2   Volumetric and planar approximations

In the generation of a particle energy spectrum the fluence contribution of each particle has to be weighted accordingly with the particle's direction; the higher the particle's angle with respect to the beam axis at a given depth, the more dose it will deposit at that depth and thus, the higher the contribution to the particle spectrum should be. Two methods that implement this were investigated: the volumetric and planar approximations. In the former, the fluence of a particle is weighted with it's track length, resulting in the so-called *track-weighted*
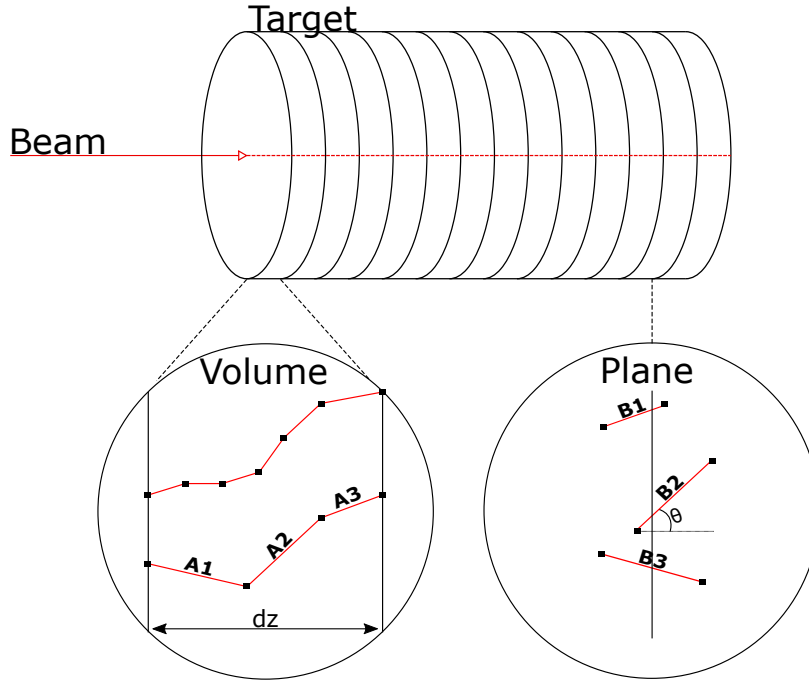
Fig. 3.1 The system geometry with visualisations of the volumetric approximation (left) and the planar approximation (right). The vectors **A** and **B** represent the relevant part of the particle phase space in order to create the volumetric and planar energy spectra, respectively.

fluence. In the latter, the particle fluence is weighted with the angle between the particle and the beam axis. Figure 3.1 gives a visual interpretation of the volumetric (left) and planar (right) approximations.

In the volumetric approximation, the cylindrical system is divided in thin disks. In each disk the depth-averaged particle energy spectra will be defined. A particle crossing a disk can undergo multiple energy loss events that will be added to the energy spectrum separately. The vector A_i represents the phase space of event i, consisting of the ion charge Z_i, the kinetic energy of the particle E_i *after* the event[4] (in MeV/u) and the distance dr_i travelled since the last energy loss event. Each energy loss event of the particle is then added to the corresponding energy spectrum with weight w_i:

$$w_{volume}^i = \frac{dr_i}{\Delta z} \tag{3.2}$$

where division by Δz, the disk thickness, is required to get the depth-averaged energy spectra in the bin. In the case displayed in figure 3.1 (left), tho bottom particle will result in three

---

[4]The particle energy that is used is in the energy spectra is not the energy after an event (E_i), but the mean energy between two consecutive events E'. This energy is approximated with linear interpolation, i.e. $E' = \frac{1}{2}(E_i + E_{i-1})$.

(a) 10 cm depth (plateau)

(b) 35 cm depth (fragment tail)
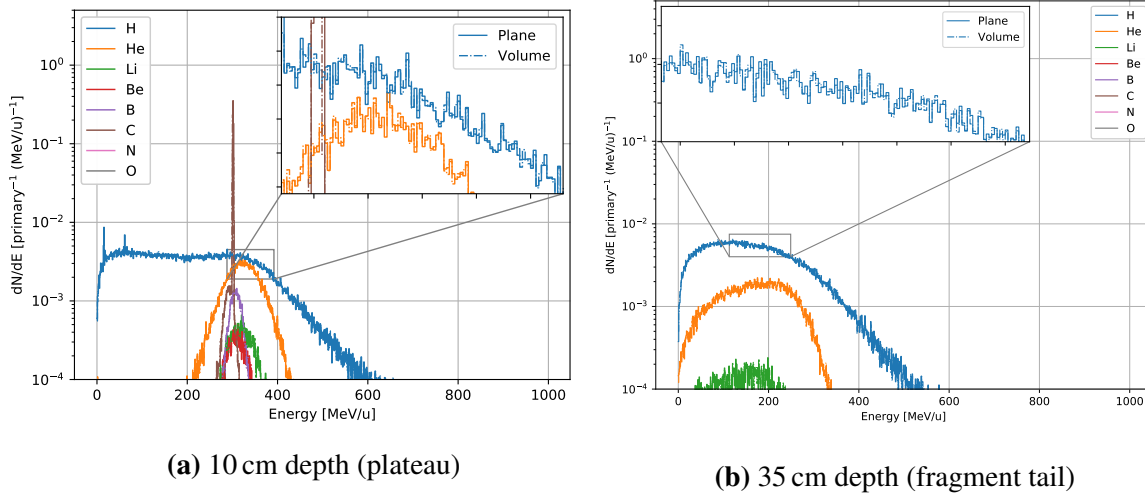
Fig. 3.2 Energy spectra for ions with $Z \leq 8$ using the plane and volume fluence estimations. Simulation of a 400 MeV/u carbon beam for 10×10^5 particles.

entries to the energy spectrum of it's ion species. Similarly, the top particle will result in six entries to the corresponding energy spectrum.

In the planar approximation the energy spectra histograms will be computed in regularly spaced planes inside the geometry. The phase space of the particle track segments crossing a plane, denoted by B, are similar to reported above. However, instead of the track length between two consecutive energy loss events, it consists of θ, the angle between the trajectory and the beam axis. The weight w_i of particle i in the energy spectra is now given by

$$w^i_{plane} = \frac{1}{|\cos \theta_i|}.$$

(3.3)

The absolute value of the angle is used to not discriminate between particles moving in the forward or backward direction.

Theoretically, both methods should give equal results if the disk thickness in the volumetric method would be chosen sufficiently small. In our case, the disk thickness and the distance between two planes are both 0.1 cm. Figure 3.2 displays the energy spectra of a 400 MeV/u carbon beam at two depths for both methods. Only small differences can be observed, but remarkably, the planar spectra show some sudden peaks, for example in the low energy region of hydrogen in figure 3.2a. This could be due to an ion that moves almost parallel to a plane, resulting in an extremely high weight.

A comparison between the methods is displayed in figure 3.3, where the percentage differences between the spectra dose and the real IDD are displayed for both methods. Evi-
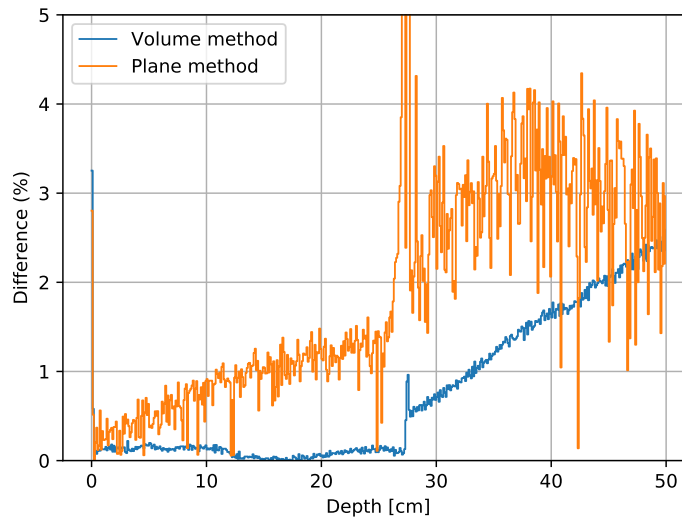
Fig. 3.3 Percentage local difference between the IDDs calculated from the energy spectra and the 'real' IDDs (from USRBIN) for both approximations. Simulation of a 400 MeV/u carbon beam of 0.5×10^6 particles.

dently, the volumetric approach yields better results, both in terms of statistical fluctuations and consistency with the real IDD. The difference before the Bragg peak is close to 0% and increases in the fragment tail. The latter is mainly due to the fact that the dose there is very low and decreasing.

Consequently, the volumetric approach has been chosen here as the preferred approximation method. All energy spectra reported in the following have been generated using this method.

3.2.3 GUI

In support of the work done here, a GUI that visualises the data output of a set of FLUKA simulations has been developed. The GUI was initially developed to provide an overview of the important processes in particle beams for educational purposes. Later, it was used to evaluate and optimise the energy spectra and IDDs generated in this project.

Figure 3.4 displays the GUI for a set of five carbon beams in a water target. The three sliders (bottom right) can be used to select a beam energy, depth and radius. The GUI consists of the following figures:

- An overview plot showing all the IDDs in the simulation set. The currently selected IDD is indicated by red. (top left figure)

- The spatial distribution of distributed dose, displayed in a two dimensional histogram. (top centre figure)

- The dose deposited as a function the distance from the beam axis on the selected depth. (top right figure)

- The energy spectra of all ion species for the selected beam energy and depth. (bottom right figure)

- The IDD computed using the energy spectra and the 'real' IDD from USRBIN for the selected beam energy. (bottom left figure)

In addition, some of the views can be altered or replaced using the buttons (bottom left). The following functionalities are introduced by the buttons

- Toggling the scale of y-axis of the energy spectra between linear and logarithmic.

- Change the selected depth to the Bragg peak centre.

- Reset the scaling on all figures to the initial state.

- Show the ratio between the 'real' IDD and the IDD derived from the energy spectra in the bottom left plot.

- Show a log file containing a summary of the settings used in the simulations.

- In separate windows, show histograms of the currently selected IDD and energy spectra with uncertainties.

- Show the buildup curves of all ion species. This will be displayed in the bottom left figure.
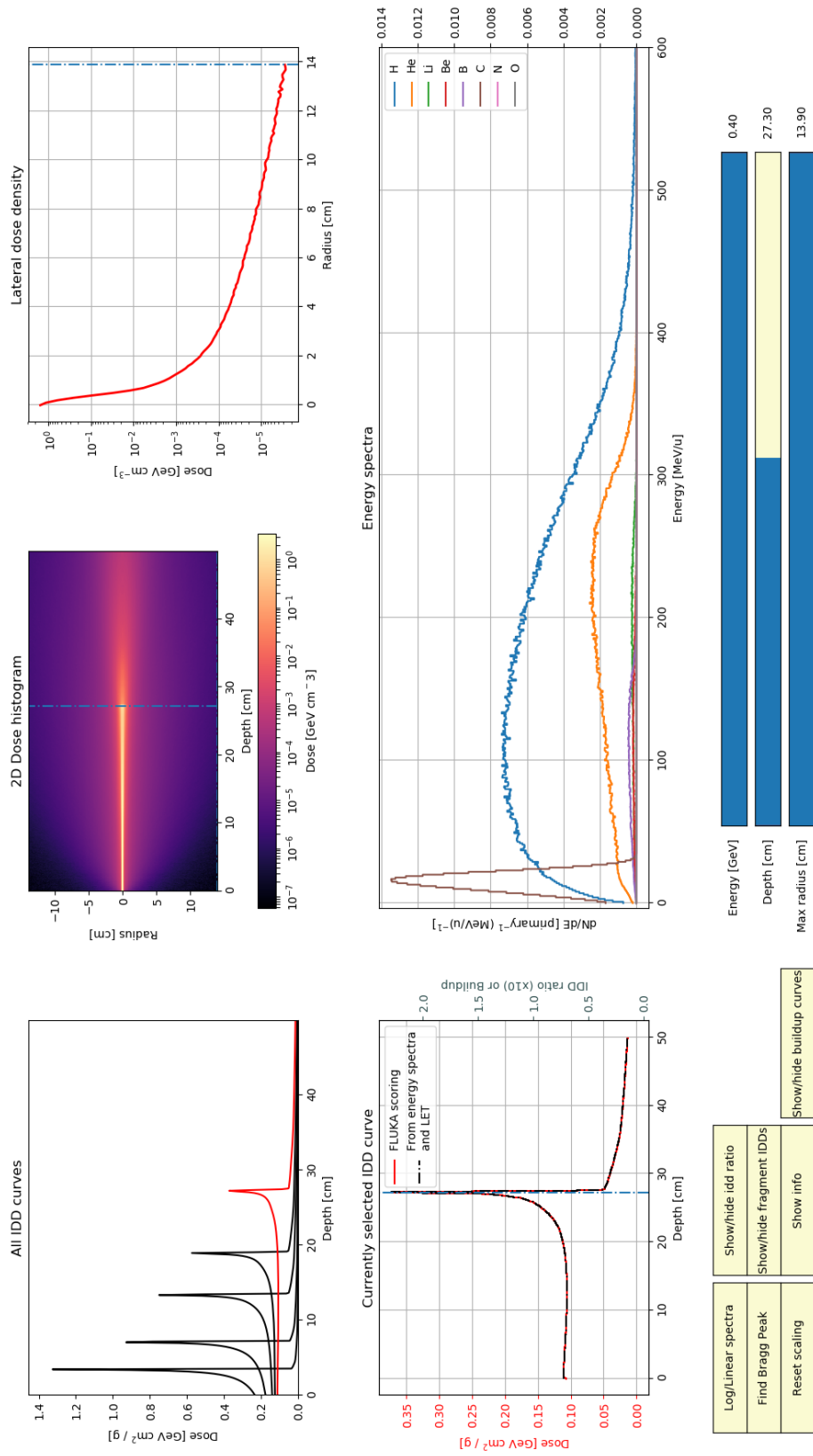
Fig. 3.4 Plotting GUI to plot data output of a group of simulations. A simulation can be selected by selecting a beam energy. In the current screen shot the beam of 400 MeV/u is selected at the Bragg peak depth.

3.3   Dose planning and radiobiology

In this work, the treatment planning system (TPS) RayStation was used to create a set of validation plans and one realistic patient treatment plan. In the treatment plans, physical dose and RBE dose were calculated and optimised in order to compare clinical results between the different base data sets. The generation of a treatment plan and the extraction of the relevant data was done in the following steps:

1. Generation of the patient case. Including, but not limited to, definition of the geometry, materials, beam set[5], target volume(s) and clinical objectives/constraints.

2. Calculation of the physical dose by the pencil beam dose engine.

3. Optimisation and RBE dose computation by the RBE dose engine based on either the old or the new energy spectra. The dose computation can be done using the classic algorithm or the low-dose approximation.

4. Computation of the physical dose by the RBE dose engine, which uses the energy spectra rather than the IDDs (see section 2.5). The resulting spectra doses can be compared to the physical dose computed by the pencil beam dose engine in order to evaluate the consistency between the energy spectra and IDDs.

5. Writing the relevant output data to text files. This includes lateral and longitudinal depth dose profiles of the physical dose, spectra dose and RBE dose.

Importantly, it was found that the differences between the old and new IDDs are small compared to the differences in the energy spectra. It is assumed that deviations in clinical outcomes between the base data sets are dominated by the energy spectra. Therefore, in every case considered here, only the new set of IDDs is implemented in the pencil beam dose engine. Consequently, the selection of beam energies as well as the computation of physical dose is based on the new IDDs. Hence, all radiobiology assessments performed here are based on changes in the energy spectra.

The next sections will describe the treatment cases that were generated, in increasing order of complexity, and the work done in each of them in support of comparisons between the old and new base data.

---

[5]The beam set is the composition of beams and the energies each beam is constituted of in the treatment plan.

3.3.1   Single energy layers

The simplest possible plan is irradiation of a rectangular volume by a mono-energetic carbon beam. In RayStation this can be set up by defining a rectangular water-filled volume and simply hand-picking a beam energy to irradiate the geometry with. Five beam energies ranging from the lowest to highest in the beam energy domain were selected. After selection of the beam energies and the computation of physical dose by the pencil beam dose engine, the plan is optimised and RBE dose is computed by the RBE dose engine using the classic algorithm (section 2.5.2) for the old and new energy spectra. The resulting RBE dose distributions can then be extracted. In this case, no work was done to compute the spectra dose, since pristine physical dose distributions were compared outside of RayStation.

3.3.2   Cubic target plan

In this treatment case, three cubic target volumes were defined on different depths inside the rectangular volume. In contrast to the single energy layer plans, the beam sets now consist of multiple spots in multiple energy layers. The resulting plans consist of 40 energy layers with around 350 spots in each layer.

In order to generate and optimise a treatment plan two clinical objectives were defined. Firstly, the plan was set to deliver a uniform dose of $200\,\text{cGy}\,(\text{RBE})$ inside each target and secondly, a distal dose fall-off to $0\,\text{cGy}$ within $1.00\,\text{cm}$ of the end of each target was demanded. The former objective is considered more important and received a weight ten times larger than the latter.

The plans were optimised for both the old and new spectra with the classical algorithm in order to compute RBE weighted dose. Figure 3.5 displays the RayStation plan evaluation of the intermediate depth target plan. The image shows the RBE dose calculated with the old energy spectra (top) and the new energy spectra (centre). Next to that, the dose difference (bottom) is shown. In addition to the RBE dose comparisons, the low-dose algorithm was used to calculate spectra dose in order to perform physical dose comparisons.

3.3.3   Realistic patient case

As the ultimate method of evaluating the impact of the new set of base data on clinical cases, a pre-existent patient case was selected and optimised on the data. Figure 3.6 displays examples of the patient modelling in RayStation. The treatment plan consists of two beam directions, as can be seen in the 3D patient model. The patient CT has been enhanced by contouring of relevant volumes in various colours. The relevant volumes are mainly risk
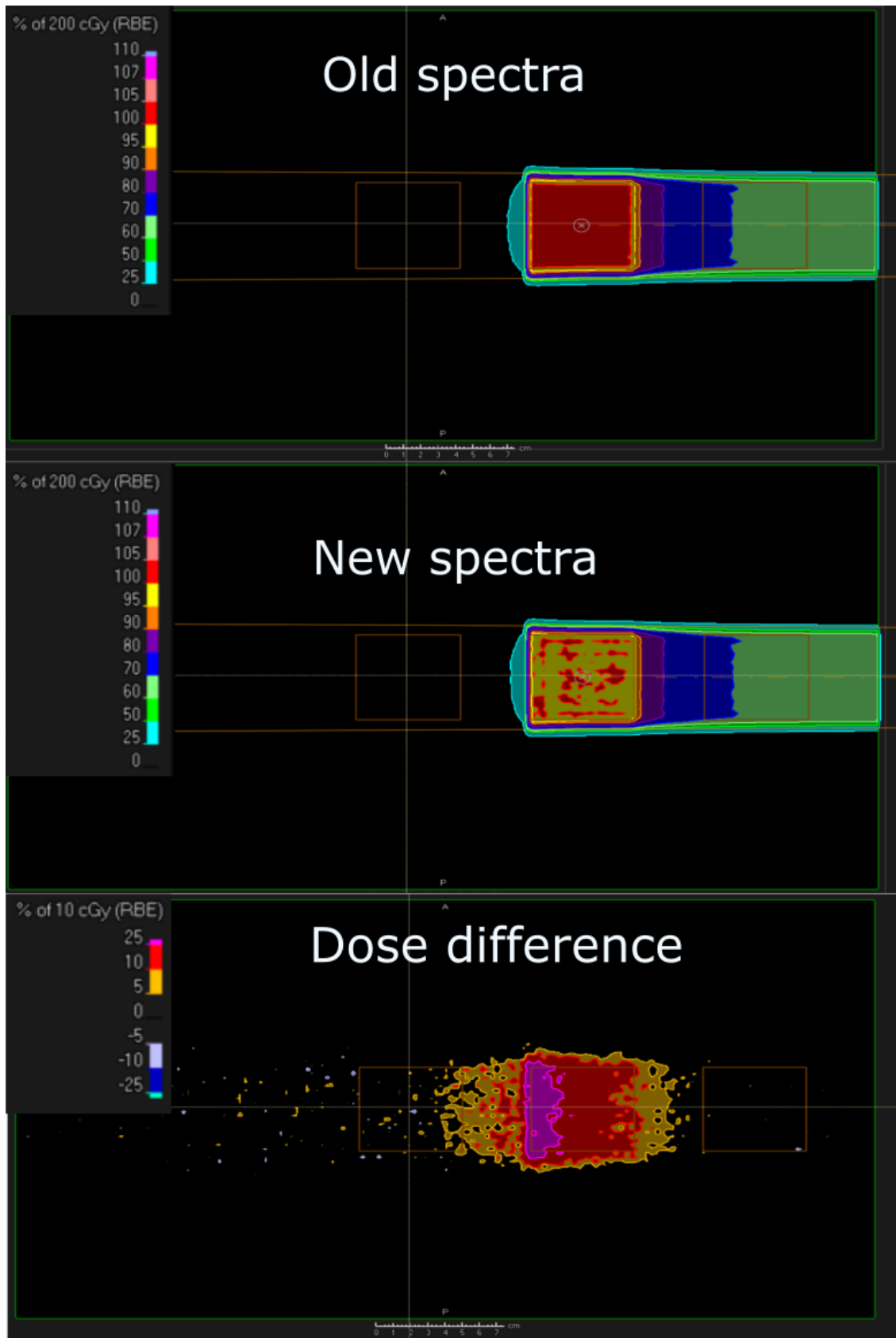
Fig. 3.5 Evaluation of the distribution of RBE weighted dose in a cubic target at intermediate depth. RBE dose computed with the old spectra (top) and the new spectra (centre) are shown. The bottom image shows the dose difference between the two plans (new - old). *Source: RayStation plan evaluation screen.*

organs and the target tumour volume. For example, the liver, duodenum, tumour, lungs and spinal chord have been contoured with purple, light green, red, blue and dark green, respectively. The target tumour volume is denoted by red.

In order to optimise and evaluate the treatment plan, several clinical objectives were imposed on the plan. With respect to the target, a uniform dose of minimally 4000 cGy with a distal fall-of to 0 cGy within 1.00 cm was requested. Additional objectives were added to spare the organs at risk, in this case the stomach and oesophagus, which were set to receive a maximum of 2600 cGy. Every physical objectives received a weight according to its importance.

In contrast to the other cases, here, both the spectra dose and the RBE computations were performed with the low-dose approximation. Figure 3.7 displays examples of the plan evaluation in RayStation The top images shows the RBE weighted dose distribution calculated with the new particle spectra. The bottom image shows the dose difference between the plans. In order to do comparative work on the RBE dose and physical dose, longitudinal and lateral line doses[6] were extracted from the treatment plans.

3.4 Intermediate conclusion

Before we begin with our coverage of the results, let us briefly summarise the work done up to this point. Firstly, methods to produce the desired data with the MC code FLUKA were defined in section 3.1, such as the determination of the physics and transport settings. Next, a framework to parse, process and visualise the FLUKA output data was introduced. This included an investigation of two fluence-weighting methods which resulted in a choice for the volumetric approximation (track-weighted fluence). Lastly, in section 3.3 several treatment cases were defined in RayStation in preparations of the data comparisons regarding physical and RBE weighted dose in clinical applications. In figures 3.5 and 3.3.3 we have seen that the new spectra lead to different RBE weighted dose results, which is something that will be studied in detail in the following sections.

3.4.1 Genericity

It is important to note that all of the methods defined in this work were developed as generic as possible in order to support any primary ion species. As a result, these methods can be, and have been, used to study irradiation with different ion species. As a demonstration of this property, appendix B displays the GUI (described in section 3.2.3) for helium beams.

---

[6]Line dose is the distribution of dose along a line.

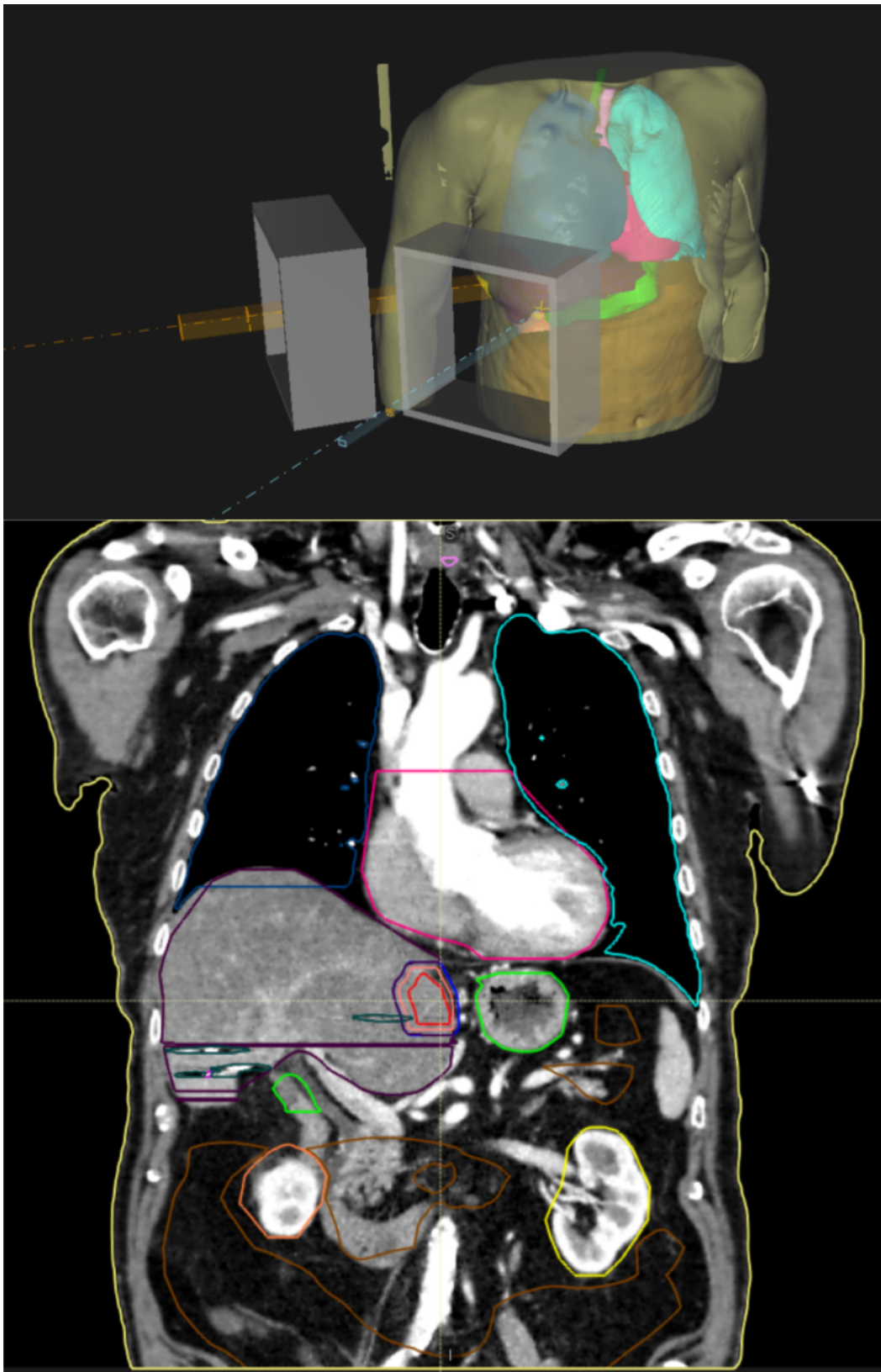**Fig. 3.6** Modelling of a patient in RayStation. Top: 3D view of the patient model. Bottom: coronal CT of the patient, which has been contoured. *Source: RayStation plan design screen.*
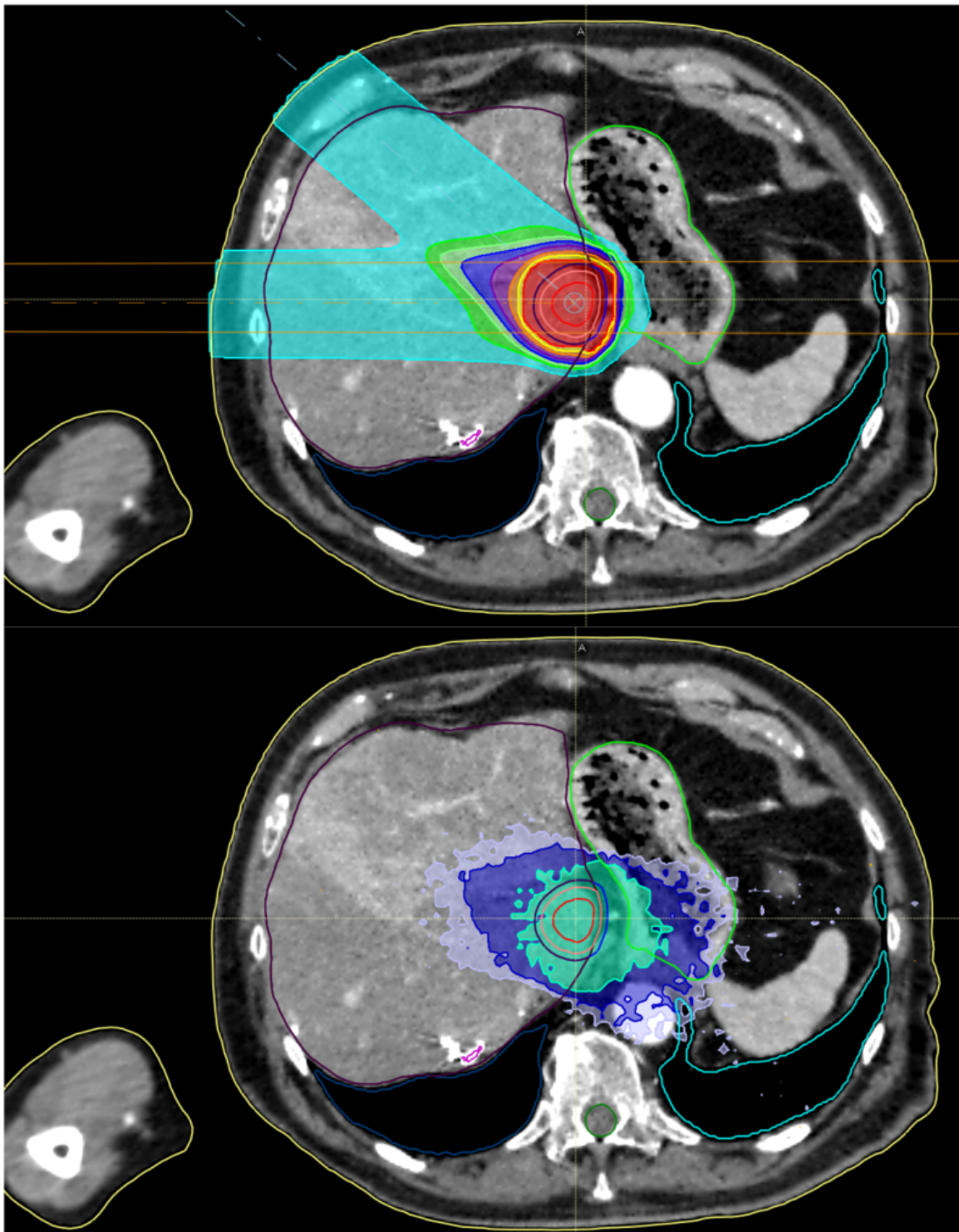
Fig. 3.7 Evaluation of the RBE dose distribution the patient plan. Top: RBE dose computed with the new spectra. Bottom: RBE dose difference between the two base data sets (new-old). *Source: RayStation plan evaluation screen.*

Chapter 4

Results

4.1 Base data

In advance of the comparative work on the pristine base data, physical dose and RBE dose in later sections, we shall look at the pristine base data as it was implemented in RayStation.

4.1.1 IDDs

Figure 4.1 displays a selection of the pristine IDDs that have been generated in this work. While the actual data extends to a depth of $100\,\mathrm{cm}$, the figure has been limited $50\,\mathrm{cm}$ to show only the Bragg peaks and part of the fragment tails. It can be seen that the peaks provide homogeneous spatial coverage of depths up to around $38\,\mathrm{cm}$. Next to that, the maxima of the peaks are captured nicely, without any notable statistical fluctuations.

4.1.2 Energy spectra

A sample of the differential energy spectra of the highest simulated beam energy can be observed in figure 4.2. The three displayed depths are $1.00\,\mathrm{cm}$, $27.30\,\mathrm{cm}$ and $35.00\,\mathrm{cm}$, corresponding to the plateau region, Bragg peak and fragment tail, respectively. As explained in earlier sections, logarithmic energy binning was applied to the fragments, while the carbon ions were binned linearly. Again, the data shows the desired statistical behaviour. Fluence of neither oxygen nor nitrogen can be observed.
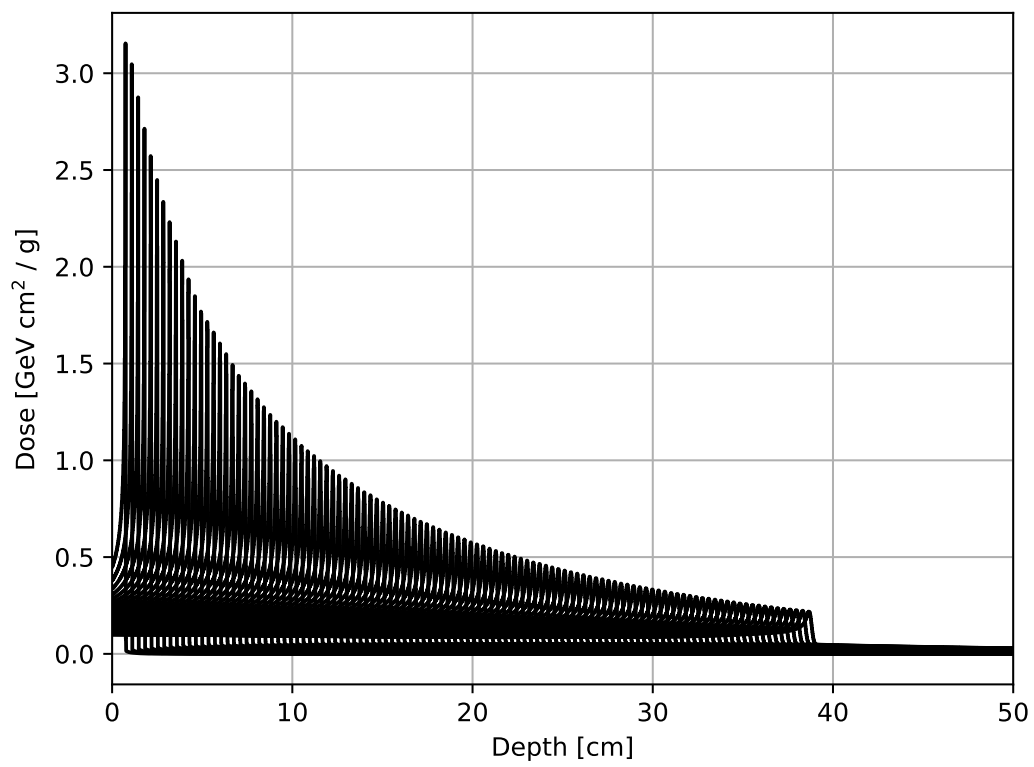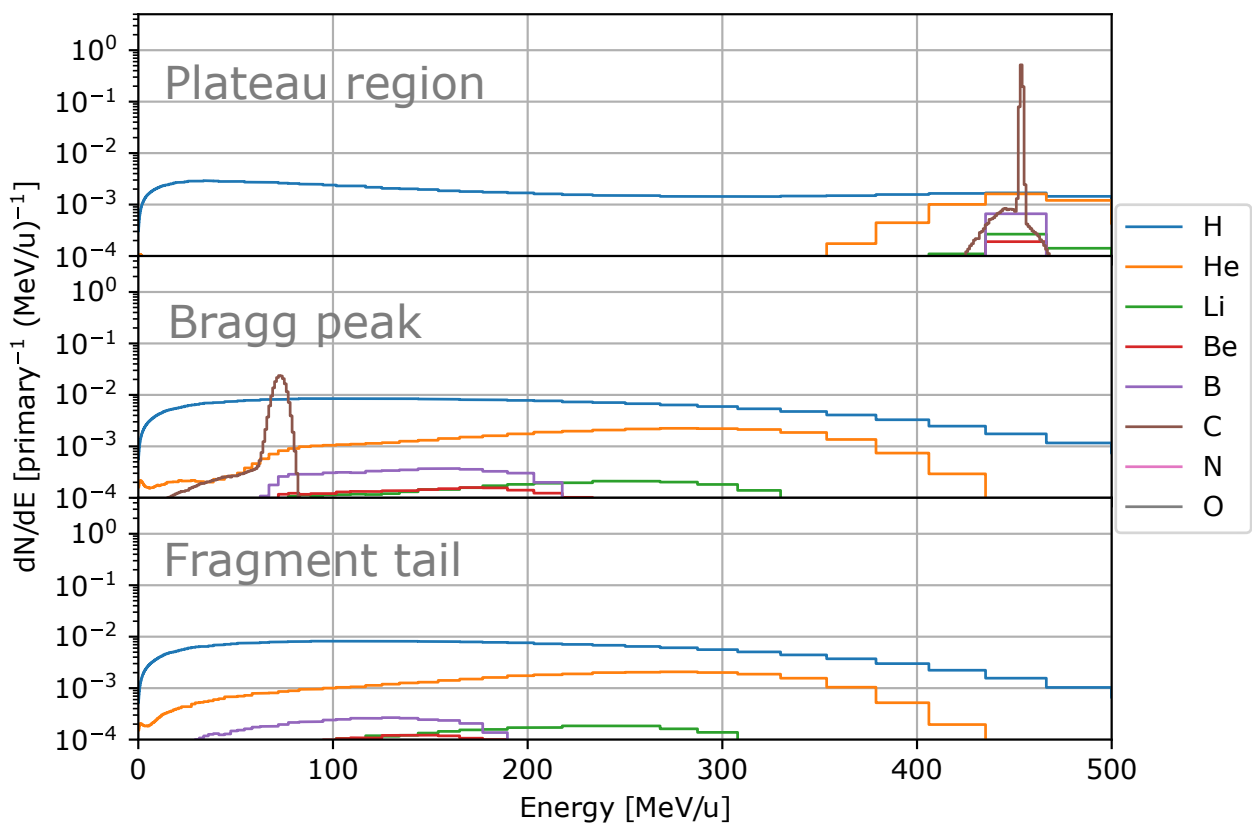
Fig. 4.1 A selection of IDDs from the final base data.

Fig. 4.2 Differential energy spectra of the 500 MeV/u carbon beam; the highest beam energy simulated in the base data.

4.2   Nitrogen and Oxygen contributions

An important development of the particle spectra is the inclusion of nitrogen and oxygen. In order to evaluate the effect of the inclusion of these fragments, we look at their dose contribution to the spectra dose. For this investigation, the beam with the highest energy in the base data has been chosen. Since this beam will have the highest buildup of secondary particles (see section 2.1.5), it will have the most significant nitrogen and oxygen contributions.

Figure 4.3 (top) shows the spectra dose of a $500 \, \text{MeV/u}$ carbon beam, including the dose contribution of every ion species up to charge $Z = 8$. No significant contribution from nitrogen or oxygen can be observed. The spectra dose from nitrogen and oxygen have been plotted separately in the middle figure, where one can observe that the dose from these fragments is indeed very low (note that the y-axis has been scaled with 10^{-3}). Lastly, the bottom figure shows the combined percentage dose contribution from nitrogen and oxygen. The dose contribution before the Bragg peak is negligibly small; 0.06% at maximum. Subsequently, in the fragment tail the contribution rises to about 0.10%, mainly due to the fact that the dose in that region is low and decreasing. Thereby, in clinical cases depths above $40 \, \text{cm}$ are rarely reached.

It can be concluded that the effect of the inclusion of oxygen and nitrogen in the fragment spectra is very limited and well below clinical uncertainties. Nevertheless, in all of the work reported in the following, nitrogen and oxygen have been included in the energy spectra.

4.3   Pristine data comparisons

In this section, physical dose comparisons between the old and new base data will be performed to assess differences in data quality. Firstly, the pristine IDDs will be compared. After that, the spectra dose will be compared to the IDDs in order to evaluate the consistency between the energy spectra and IDDs.

4.3.1   IDDs

Figure 4.4 (top) shows the relative dose distribution of an old and a new IDD for two beam energies. The bottom figures show the percentage difference between the IDDs in the top figure. Note that, due to the fact that the beam energies are not precisely equal, there is a range difference between the peaks, causing a large peak in the bottom figures at the Bragg peak depth. Thus, this is not an effect of data discrepancies.

Evidently, the new IDDs are much smoother than the old IDDs. This can be observed especially in the right inset, where the new IDD shows much less statistical fluctuations. The

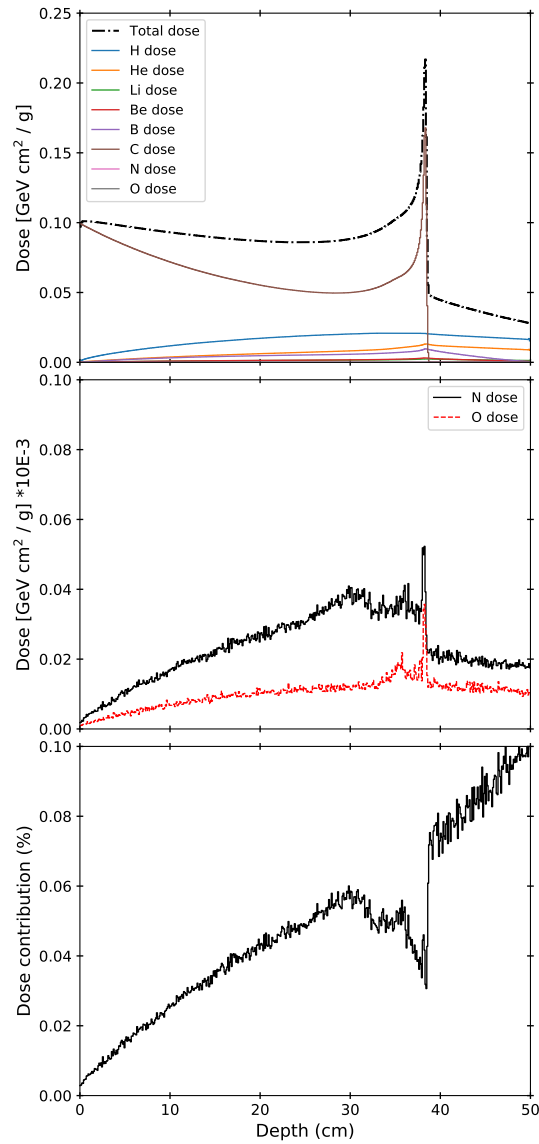**Fig. 4.3** Top: spectra dose, including the contribution of ion species. Centre: dose distributed by nitrogen (black, solid) and nitrogen (red, dotted). Bottom: combine percentage contribution to the total dose by nitrogen and oxygen.
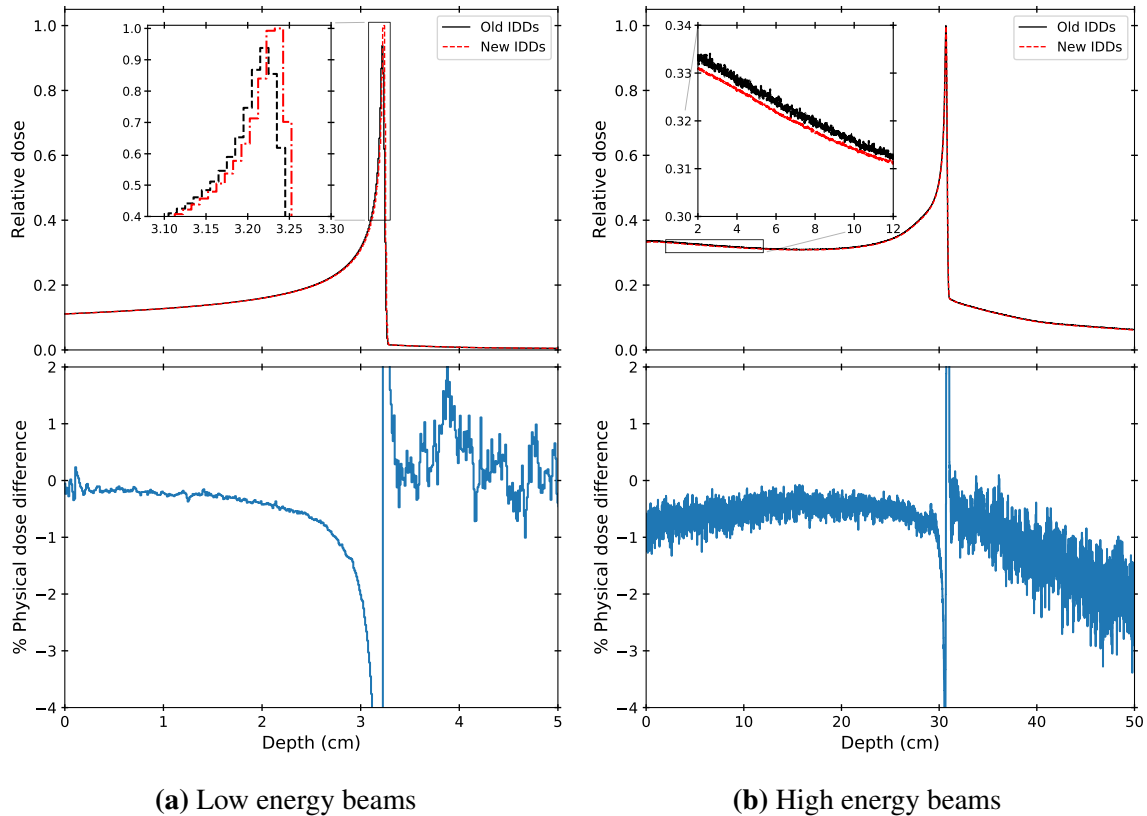
(a) Low energy beams   **(b)** High energy beams

Fig. 4.4 Top: relative physical dose from the old (black, solid) and new (red, dotted) IDDs. Bottom: the percentage dose difference between the old and new IDDs. This is shown for a $114\,\mathrm{MeV/u}$ (left) and a $430\,\mathrm{MeV/u}$ (right) carbon beam. The x-axis is shared between the top and bottom figures.

main reasons for the decrease in statistical fluctuations are the detailed handling of energy loss, as explained in section 3.1.1.1.

In the low energy case (left), it can be observed that the differences between the idds are very small and seem to be of statistical nature. Before the peak, the difference is smaller than around 0.25%, and even after the peak, where the dose is very low, the difference is never more than 1%. In the high energy case (right), however, larger variations can be observed. Before the Bragg peak, the new IDD is systematically $0.5 - 1\%$ lower than the old IDD and in the fragment tail, the new IDD is increasingly lower than the old IDD. This difference can be explained with the fact that in the new IDD simulations electrons and positrons were created and transported, causing some of these particles to escape the scoring geometry. Obviously, dose deposited by particles outside of the scoring volume will be excluded from the IDDs.

4.3.2 Spectra dose

If the energy spectra are consistent with the IDDs, all deposited dose present in the IDDs should also be present in the energy spectra. Hence, in order to test the consistency between the energy spectra and the IDDs, the spectra dose has been computed and compared to the IDDs.

A low, intermediate and high beam energy IDD were selected from the base data. Subsequently, the spectra dose for that energy was calculated for the old and new spectra. If the selected beam energy was not directly present in the energy spectra, it was obtained by interpolation of the existing spectra. For completeness this was done for both the old and the new IDDs. The results reported here, however, include only the comparisons to the old IDDs. The comparisons with the new IDDs can be viewed in appendix A.

The results are displayed in 4.5, where the top plots display the spectra doses and IDD, and the bottom plots display the percentage difference between IDD and the spectra doses. Importantly, in the bottom plots, the dose difference shows a sudden spike around the Bragg peak. This is due to the fact the the depth resolution of the energy spectra is 1.0 mm, while the resolution of the IDDs is 0.1 mm. To fix this, the energy spectra are interpolated in the depth dimension, causing the Bragg peak to be 'smeared out'. This effect can be observed in more detail in the insets in the relative dose plots.

The consistency of the new spectra dose is very good for all energies. Both before and after the Bragg peak region, the dose difference is close to 0%. Only in very low-dose regions, far in the fragment tail of the low and middle energy plots, some deviations can be observed. The old spectra seem to be less consistent with the IDDs. Before the Bragg peak the old spectra dose behaves pretty well, and only for high beam energy the spectra dose shows some discrepancies up to approximately 5%. In the fragment tails, however, the dose seems to be underestimated significantly. The reason for this underestimation is that in the simulation of the old energy spectra, the scoring radius was only 5 cm[1]. Due the lateral beam spread in the fragment tail, a significant portion particle flux has not been detected. Hence, a large portion of dose is missing from the spectra dose.

From these results, it can be concluded that the main source of differences in radiobiology will be due to the energy spectra. Therefore, it has been decided that the comparative work performed in RayStation will focus on the impact of differences in the energy spectra.

---

[1]The scoring radius was 5 cm, for historic reasons, in order to conform to a reference RBE dose computation.
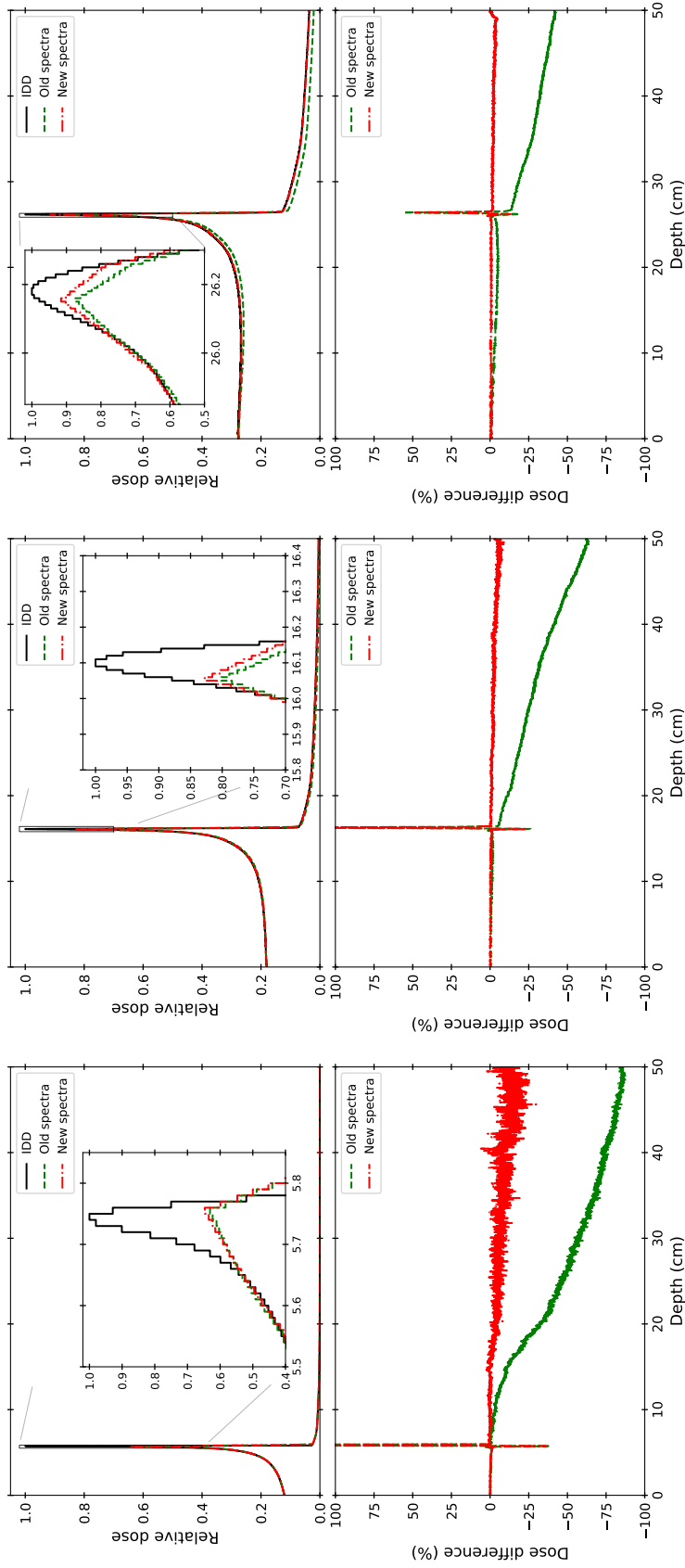
(a) 158 MeV/u beam.

(b) 289 MeV/u beam.

(c) 389 MeV/u beam.

Fig. 4.5 Top figures: relative physical dose from the **old** IDDs (black), old energy spectra (green) and new energy spectra (red). Bottom figures: percentage difference between the IDD and spectra dose for the old energy spectra (green) and the new energy spectra (red). The x-axis is shared between the top and bottom figures.

4.4 Treatment plan comparisons in RayStation

In this section we will study the impact of the reported differences in the base data on the physical and RBE weighted dose in a set of treatment plans in RayStation. The generation of the treatment plans has been described in section 3.3.

Importantly, while previous sections were specifically aimed to draw conclusions regarding the quality of the data, this section serves more as an assessment of the differences in radiobiology between the old and the new base data. Hence, this section does not aim to make statements about whether the new base data is 'good' or 'bad'.

4.4.1 Physical dose

4.4.1.1 Cubic target

Figure 4.6 displays comparisons of the spectra dose extracted from the cubic treatment plan as described in section 3.3.2. In figure 4.6a comparisons of the line dose along the beam axis are shown. Figure 4.6b displays comparisons of the lateral line dose through the centre of the target.

The results are in agreement with what was seen in section 4.3.2. In the shallow target, the spectra doses are almost equal. In the deeper targets, however, higher dose differences between the old and new spectra can be observed. Especially in the fragment tail, where the old spectra dose is significantly lower than the new spectra dose. In the centre of the deep target, the dose difference reaches 5%, corresponding to 2.5 cGy. Near the distal edge of the target, the dose difference difference rises up to 5 cGy.

4.4.1.2 Realistic patient

Figure 4.7 displays the spectra dose comparisons extracted from the real patient case. As was seen in earlier sections, the spectra dose from the old energy spectra underestimate the physical dose with respect to the new energy spectra. In the centre of the tumour, the lateral dose difference is around 2%. The longitudinal line dose, however, shows that the dose difference increases to values above 10%. The absolute physical dose difference is never greater than 60 cGy.
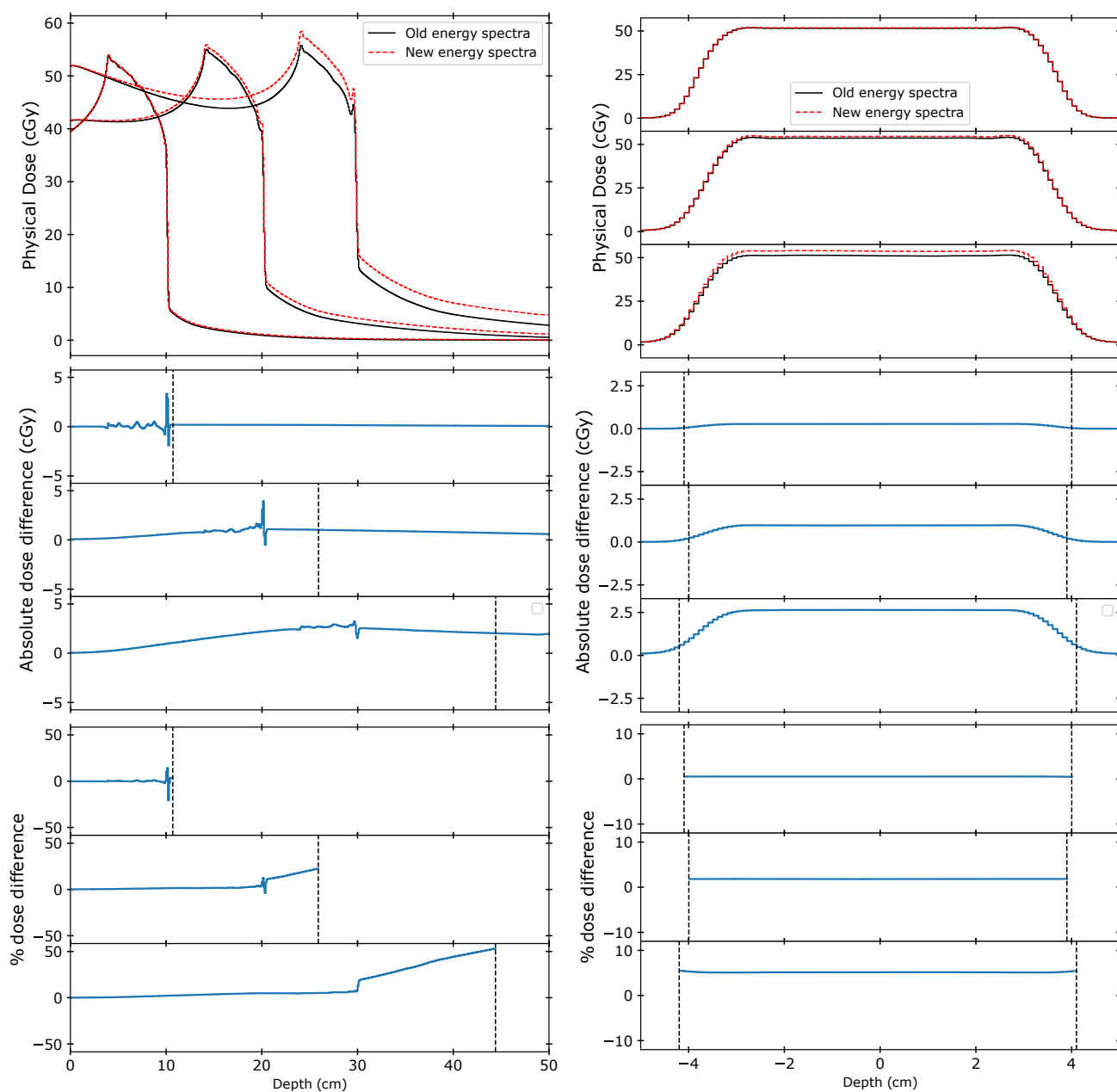
(a) Line dose along the beam axis.

(b) Lateral line dose through the centre of the target.

Fig. 4.6 Spectra dose comparisons for cubic target plans at three depths. Top: spectra dose profiles of the old (black, solid) and the new (red, dotted) spectra. Centre: Absolute dose differences. Bottom: percentage dose differences. The figures divided in three subfigure (all except the top left figure) display results corresponding to the shallow, mid and deep target plans (from top to bottom). The vertical dotted black lines indicates the 20% of maximum dose boundary, beyond which the percentage dose difference has been cut off.
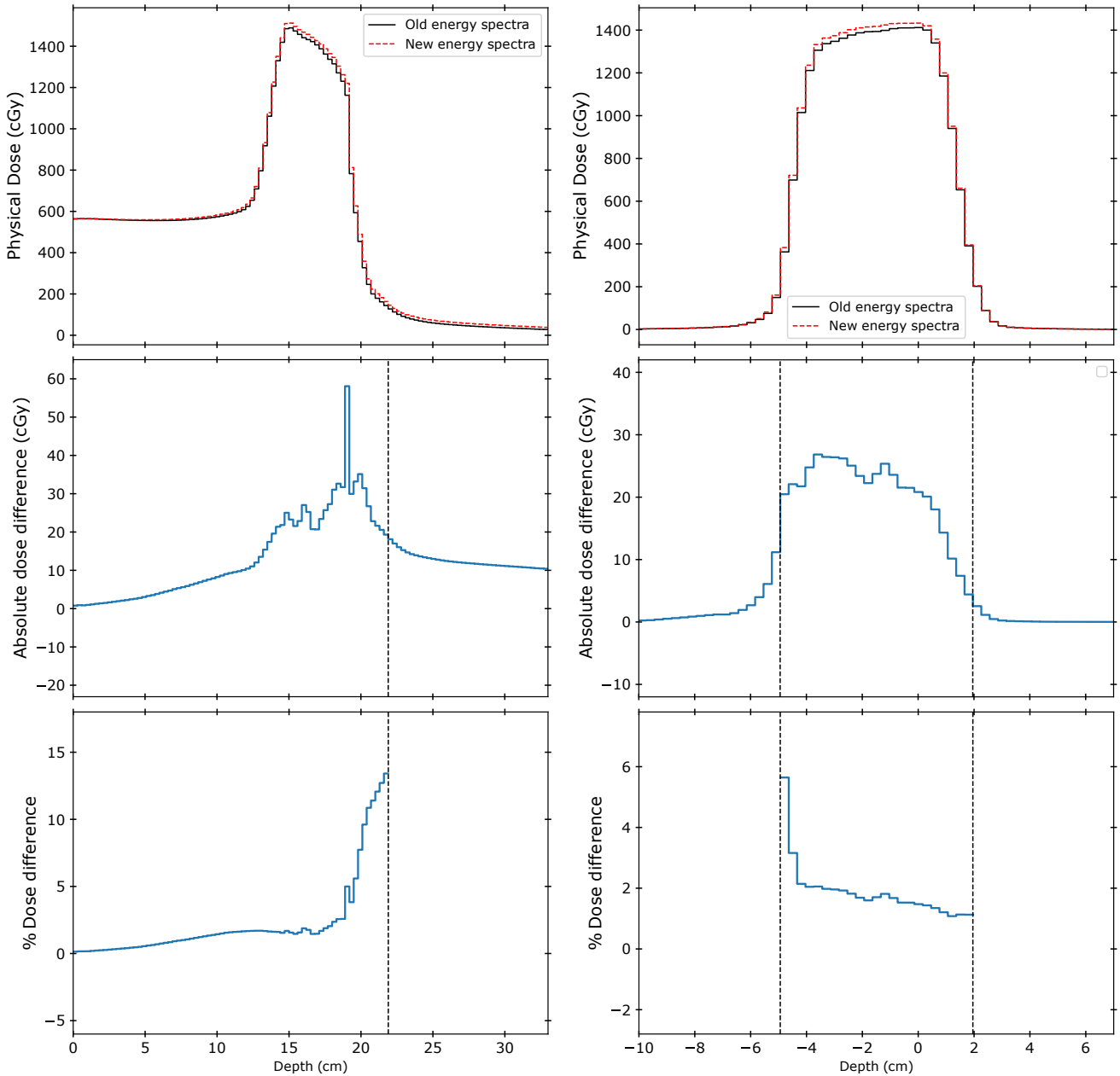
(a) Line dose along the transversal beam axis.

(b) Lateral line dose through the tumour centre.

Fig. 4.7 Spectra dose comparisons for the real patient case. Top: spectra dose profiles of the old (black, solid) and the new (red, dotted) spectra. Centre: Absolute dose differences. Bottom: percentage dose differences. The vertical dotted black lines indicates the 20% of maximum dose boundary, beyond which the percentage dose difference has been cut off.

4.4.2   RBE weighted dose

4.4.2.1   Single Energy Layers

Figure 4.8 displays comparisons of the RBE dose extracted from the single energy layer treatment plans as described in section 3.3.1. In figure 4.8a, comparisons of the line dose along the beam axis are shown. Figure 4.8b displays comparisons of the lateral line dose through the centre of the target.

Looking at the line dose along the beam axes in figure 4.8a, the results show reasonable agreement between the RBE doses. The dose difference before the target is around 0%. Subsequently, inside the peak region a maximum difference of around 2 cGy is reached. Looking at the lateral dose distribution in figure 4.8a, it can be observed that higher beam energies lead to increased dose differences inside the target. For the highest beam energy, the RBE dose difference inside the target is around 2%.

Remarkably, the RBE dose computed using the new energy spectra lies below the RBE dose from the old energy spectra, whereas previously, we saw that the new spectra dose is systematically higher than the old spectra dose. The cause of this effect will be explained in the next section.

4.4.2.2   Cubic target

The resulting RBE dose comparisons of the cubic treatment plans, as described in section 3.3.2, are displayed in figure 4.9. The results are in similar to what was seen in section 4.4.2.1. Whereas the RBE doses in the shallow target are very similar, larger deviation between the doses can be observed in the deeper targets. In the deep target, for example, the dose difference in the centre of the target is around 2% and up to 5% at the distal edge of the target.

It can clearly be seen that the RBE dose from the new energy spectra lies below the RBE dose from the old spectra. This is an effect caused by the increased scoring radius in the simulation of the new energy spectra with respect to the old spectra. Due to the increased scoring radius, there is a higher relative contribution of low LET particles in the energy spectra. The RBE dose engine, which samples particles from the energy spectra in order to compute the biological effect, now has a higher chance to sample a low mass particle with low biological effect. Thus, the RBE computed from the new energy spectra is decreased with respect to the old spectra. This is especially relevant at higher depths, where the number of low mass particles in the outer region of the geometry is large due to the lateral beam spread.
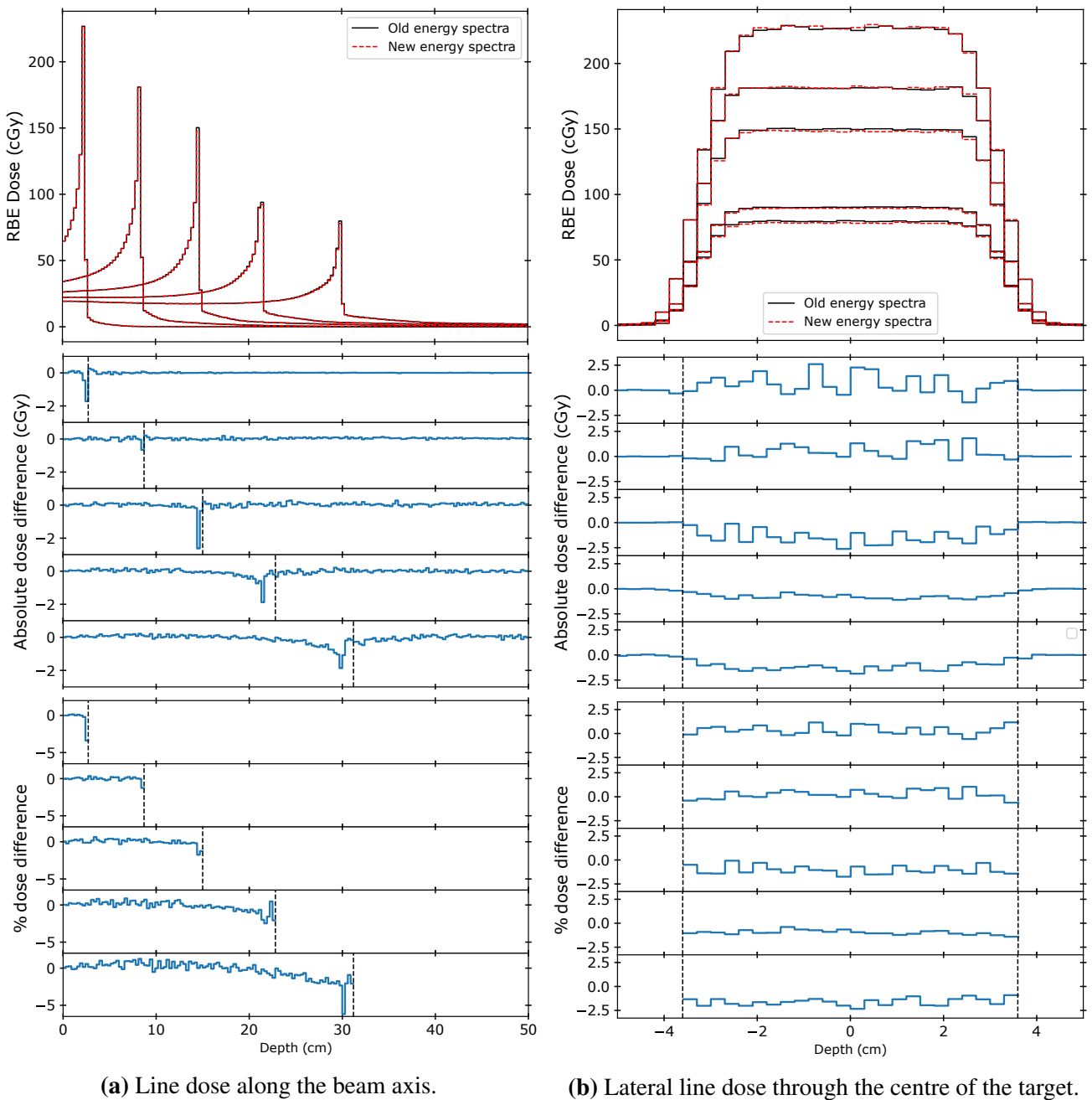
(a) Line dose along the beam axis.

(b) Lateral line dose through the centre of the target.

Fig. 4.8 RBE weighted dose comparisons for five single energy layers. Top: RBE dose calculated with the old (black, solid) and the new (red, dotted) spectra. Centre: Absolute RBE dose differences. Bottom: percentage RBE dose differences. The figures divided in five subfigures (all except the top figures) display results in increasing order of beam energy (from top to bottom). The vertical dotted black lines indicates the 20% of maximum dose boundary, beyond which the percentage dose difference has been cut off.
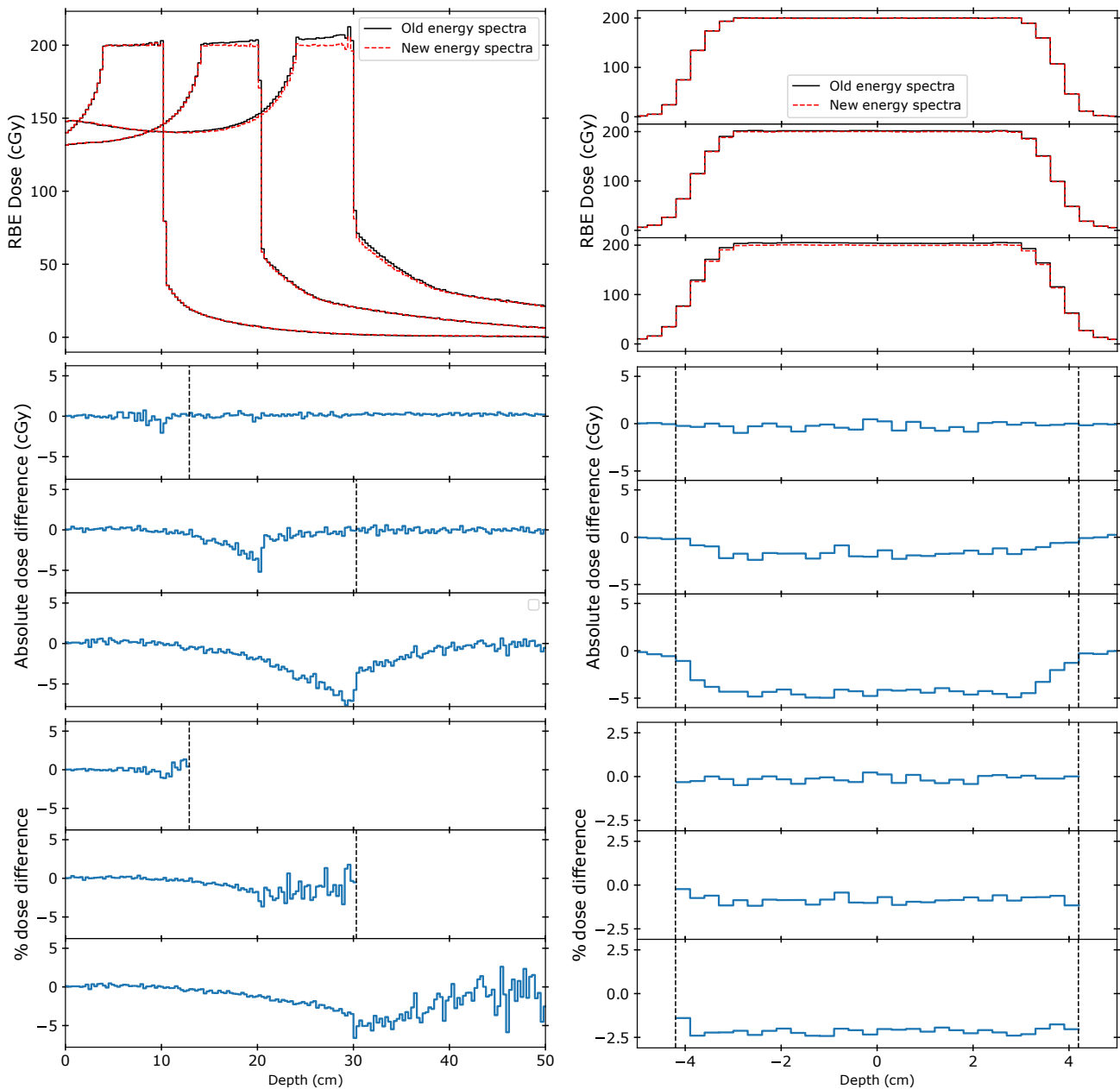
(a) Line dose along the beam axis.

(b) Lateral line dose through the centre of the target.

Fig. 4.9 RBE weighted dose comparisons for cubic target plans at three depths. Top: RBE dose calculated with the old (black, solid) and the new (red, dotted) spectra. Centre: Absolute RBE dose differences. Bottom: percentage RBE dose differences. The figures divided in three subfigures (all except the top left figure) display results corresponding to the shallow, mid and deep target plans (from top to bottom). The vertical dotted black lines indicates the 20% of maximum dose boundary, beyond which the percentage dose difference has been cut off.

4.4.2.3   Realistic patient

The final RBE dose comparisons between the old and new energy spectra for the realistic patient case are shown in figure 4.10. The results are similar to the results seen in the simple treatment plans in sections 4.4.2.1 and 4.4.2.2.

In the centre of the tumour (figure 4.10b), the dose difference is approximately 1% and never higher than $60\,\mathrm{cGy}$. The line dose along the beam axis, however, shows that differences of up to 3.5% can be reached in the distal region of the target.

From these results, it can be concluded that the new energy spectra can cause non negligible changes in the estimations of delivered RBE dose. In some regions, the percentage difference in RBE dose even approach clinical uncertainty limits. Because of this, clinics may want to revalidate their RBE dose prescriptions.

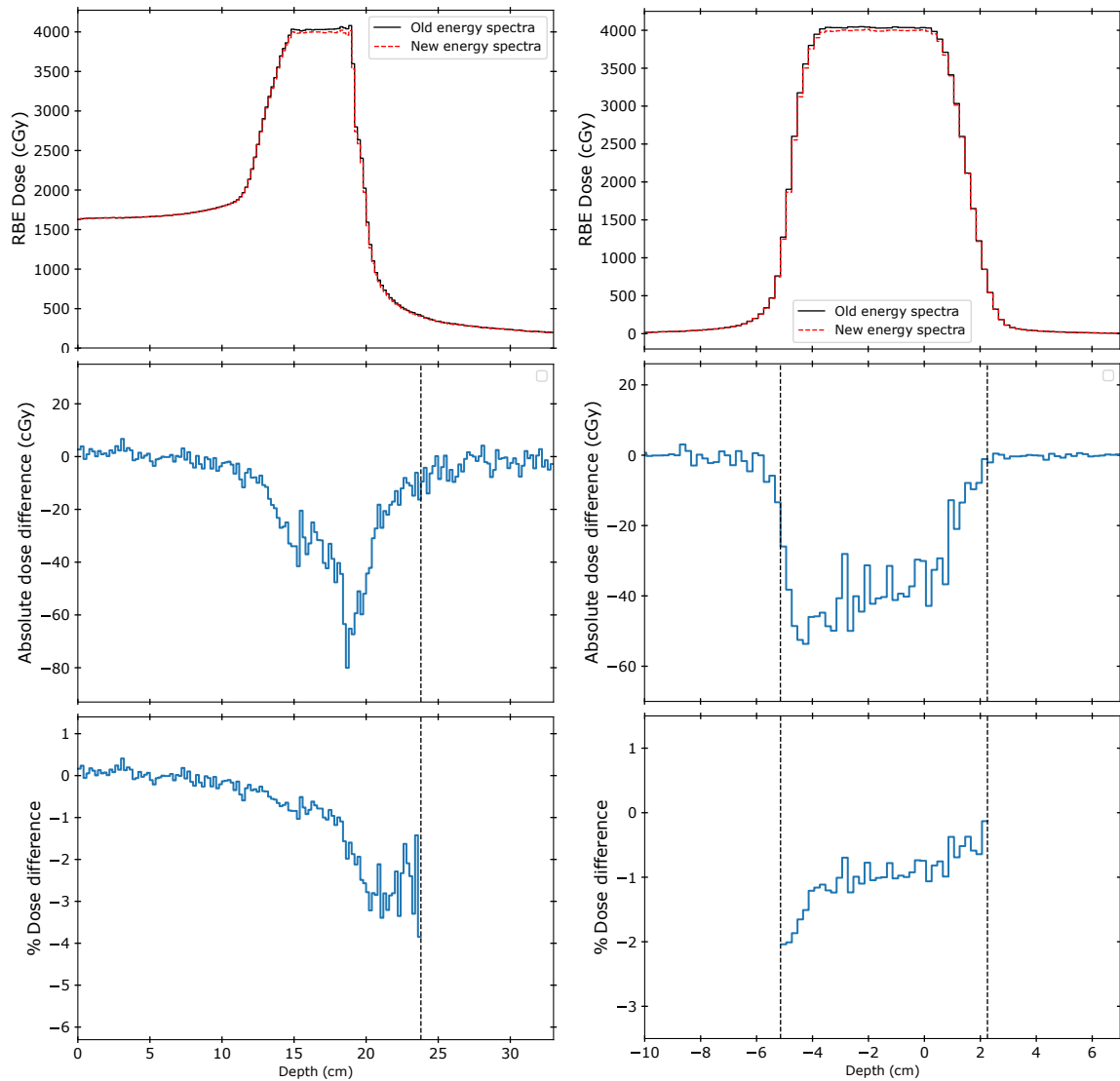**(a)** Line dose along the transversal beam axis. **(b)** Lateral line dose through the centre of the tumour.

Fig. 4.10 RBE weighted dose comparisons for the real patient case. Top: RBE dose calculated with the old (black, solid) and the new (red, dotted) spectra. Centre: Absolute RBE dose differences. Bottom: percentage RBE dose differences. The vertical dotted black lines indicates the 20% of maximum dose boundary, beyond which the percentage dose difference has been cut off.

Chapter 5

Conclusion and discussion

Detailed calculations of the physical dose and biological effect of ionising radiation are vital in radiotherapy. This is generally done by the dose engine in a treatment planning system (TPS), which relies on base data sets consisting of IDDs and differential particle spectra. Due to the evolution of radiotherapy and simulation methods, the base data of the RayStation carbon dose dose engine needs to be re-evaluated and optimised.

In this study, the Monte Carlo (MC) code FLUKA has been used to generate a new, optimised set of base data in support of the RayStation carbon dose engine. Notable changes with respect to the old base data are, firstly, inclusion of the target-recoils nitrogen and oxygen in the differential particle spectra. Secondly, optimised transport settings, such as detailed handling of energy loss and the creation and transport of electrons, were applied to the FLUKA simulations. Thirdly, the differential particle spectra were computed using the volumetric fluence estimation method.

Through a series of comparisons between the old and new data, the data has been validated and the effect on clinical applications has been determined. The new base data has been identified to be more consistent and less subject to statistical fluctuations. On top of that, non negligible changes in physical and RBE weighted dose in treatment plans were found. The behaviour of the old base data is to conform with the previous reference. If a clinic decides to update to the new base data, it may require them to revalidate their dose prescriptions and machine models.

Some additional findings can be reported. Firstly, no clinically relevant dose contributions of nitrogen and oxygen were found. The target-recoils have, however, been kept in the base data for completeness reasons. Secondly, due to the transport of electrons and positrons, dose-levels in the IDDs have dropped slightly. The changes are within 1% in the plateau region and 3% in the fragment tail.

The findings could be further investigated by studying the influence of the different ion species on the physical and RBE weighted dose in RayStation. Here, the dose contributions of oxygen and nitrogen were only studied in the pristine spectra dose outside the scope of RayStation. However, the large biological effect of these particles could lead to enhanced RBE weighted dose contributions. Another limitation of this study is the energy binning of the differential particle spectra, which was taken over from the old particle spectra without revision. Further investigations will have to determine if the energy binning can be optimised.

A possibly important effect of this work which has not been studied here, is the fact that the increased geometry radius in the energy spectra simulations could have a negative effect on dose calculations in treatment cases with very small fields, such as eye treatment. Due to the increased radius, a larger contribution of low mass and low biological effect particles will be present in the energy spectra. In small fields, this could lead to the decrease of predicted dose levels. In future work, it is important that this effect is studied.

This study has paved a way for several follow up studies, which are being set up by RaySearch Laboratories. This includes:

(i) Further validations of the base data by the deployment of secondary Monte Carlo transport software. For this work, the MC code PHITS has been selected [18].

(ii) The generation of radius-dependent energy spectra in order to be able to associate each Gaussian distributions of the nuclear halo with different particle species. This is sometimes in literature referred to as *the tri-chrome model* [7].

(iii) Research to completely discard the IDDs from RayStation. This has become a possibility due to the increased consistency between the IDDs and energy spectra in the new base data. Consequently, the pencil beam dose algorithm could solely rely on the spectra dose, rather than the IDDs.

The new base data generated in this work have been implemented in a research version of RayStation and will be considered for implementation in a clinical version. If so, the base data will be used to calculate physical and RBE weighted dose in clinical treatment plans.

Helium treatment planning

As a result of the efforts made to make the work as generic as possible, it can be reported that the methods developed in this study have been used to generate a set of helium base data in favour of the helium dose engine, which is currently being developed by RaySearch Laboratories.
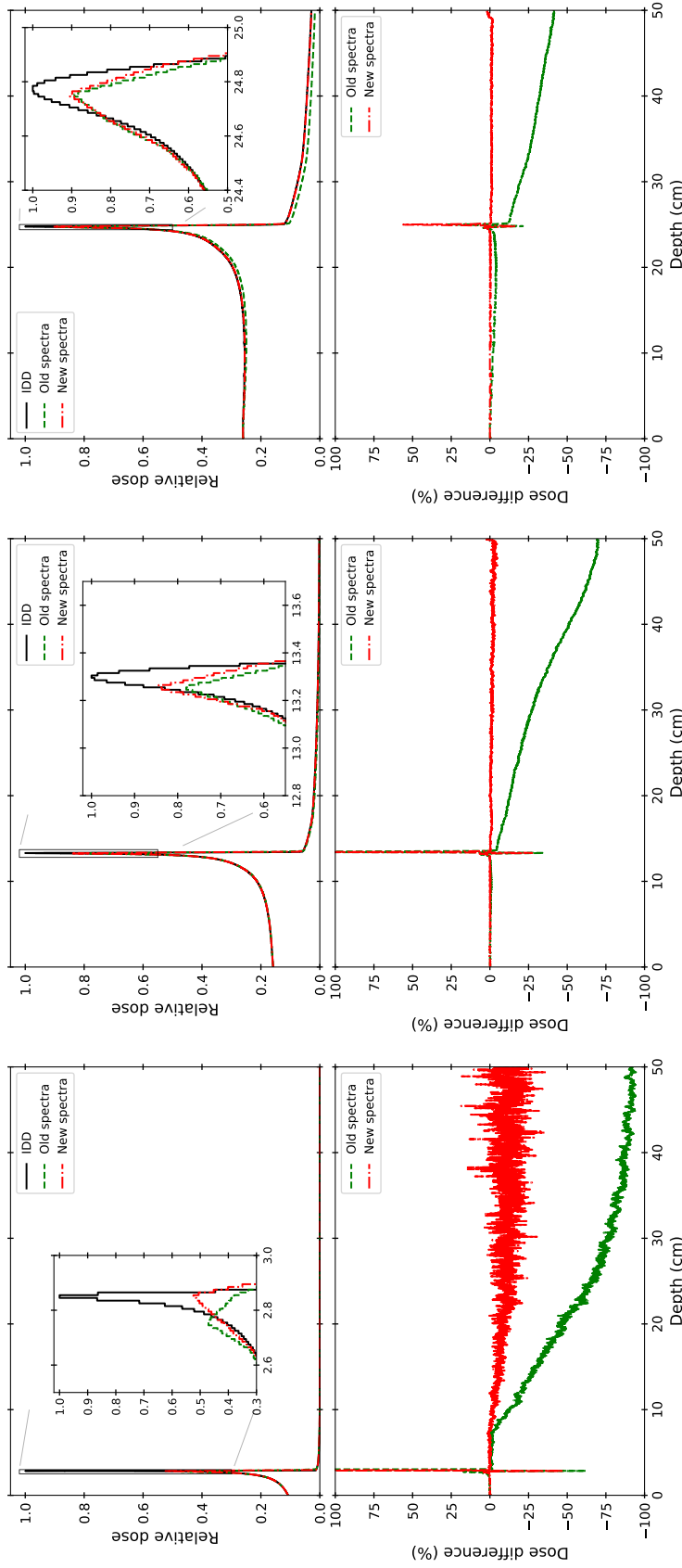
References

[1] authors (employees of RaySearch Laboratories), V. (2018). Raystation 8b reference manual. 40.

[2] Carabe, A. (2013). Radiobiology of proton and carbon ion therapy. In Ma, C. and Lomax, T., editors, *Proton and Carbon Ion Therapy*, chapter 5, pages 71–98. CRC Press.

[3] Elsässer, T., Gemmel, A., Scholz, M., Schardt, D., and Krämer, M. (2009). The relevance of very low energy ions for heavy-ion therapy. *Physics in medicine and biology*, 54(7):N101–N106.

[4] Gottschalk, B. (2012). Fermi-eyges theory. In *Proton and Carbon Ion Therapy*, chapter 4. Techniques of Proton Radiotherapy: Transport Theory, Harvard University Laboratory for Particle Physics and Cosmology, 18 Hammond St., Cambridge.

[5] Grant, J. D. and Chang, J. Y. (2014). Proton-Based Stereotactic Ablative Radiotherapy in Early-Stage Non-Small-Cell Lung Cancer. *BioMed Research International*, 2014:1–7.

[6] Inaniwa, T., Furukawa, T., Kase, Y., Matsufuji, N., Toshito, T., Matsumoto, Y., Furusawa, Y., and Noda, K. (2010). Treatment planning for a scanned carbon beam with a modified microdosimetric kinetic model. *Physics in medicine and biology*, 55:6721–6737.

[7] Inaniwa, T. and Kanematsu, N. (2015). A trichrome beam model for biological dose calculation in scanned carbon-ion radiotherapy treatment planning. *Physics in Medicine and Biology*.

[8] Inaniwa, T., Kanematsu, N., Hara, Y., Furukawa, T., Fukahori, M., Nakao, M., and Shirai, T. (2014). Implementation of a triple Gaussian beam model with subdivision and redefinition against density heterogeneities in treatment planning for scanned carbon-ion radiotherapy. *Physics in Medicine and Biology*.

[9] Jäkel, O. (2012). Lecture notes in advanced physical methods in radiotherapy - energy loss of ions.

[10] Kramer, M. and Scholz, M. (2000). Treatment planning for heavy-ion radiotherapy: Calculation and optimization of biologically effective dose. *Physics in Medicine and Biology*.

[11] Krämer, M. and Scholz, M. (2006). Rapid calculation of biological effects in ion radiotherapy. *Physics in Medicine and Biology*.

[12] Ma, C.-M., Lomax, T., R Hendee, W., and Amos, R. (2013). Proton and carbon ion therapy. *Medical physics*, 40:057301.

[13] Parodi, K., Mairani, A., Brons, S., Hasch, B. G., Sommerer, F., Naumann, J., Jäkel, O., Haberer, T., and Debus, J. (2012). Monte Carlo simulations to support start-up and treatment planning of scanned proton and carbon ion therapy at a synchrotron-based facility. *Physics in Medicine and Biology*, 57(12):3759–3784.

[14] Schardt, D., Elsässer, T., and Schulz-Ertner, D. (2010). Heavy-ion tumor therapy: Physical and radiobiological benefits. *Rev. Mod. Phys.*, 82:383–425.

[15] Scholz, M., Kellerer, A. M., Kraft-Weyrather, W., and Kraft, G. (1997). Computation of cell survival in heavy ion beams for therapy: The model and its approximation. *Radiation and Environmental Biophysics*, 36(1):59–66.

[16] Weyrather, W. K. and Debus, J. (2003). Particle beams for cancer therapy. *Clinical Oncology*, 15(1).

[17] Weyrather, W. K. and Kraft, G. (2004). RBE of carbon ions: Experimental data and the strategy of RBE calculation for treatment planning. In *Radiotherapy and Oncology*.

[18] Yang, Z.-y., Tsai, P.-E., Lee, S.-C., Liu, Y.-C., Chen, C.-C., Sato, T., and Sheu, R.-J. (2017). Inter-comparison of Dose Distributions Calculated by FLUKA , GEANT4 , MCNP, and PHITS for Proton Therapy. *EPJ Web of Conferences (ICRS-13 & RPSD-2016)*, 153:04011.

[19] Ytre-Hauge, K. S. (2016). Lecture notes in particle therapy.

Appendix A

Pristine spectra dose

Figure A.1 displays comparisons between the spectra dose and the old IDDs. This was seen in section 4.3.2 for the new IDDs, which showed similar results.

Fig. A.1 Top figures: relative physical dose from the **new** IDDs (black), old energy spectra (green) and new energy spectra (red). Bottom figures: percentage difference between the IDD and spectra dose for the old energy spectra (green) and the new energy spectra (red). The x-axis is shared between the top and bottom figures.

(a) 106 MeV/u beam.

(b) 257 MeV/u beam.

(c) 376 MeV/u beam.

Appendix B

GUI for helium beams
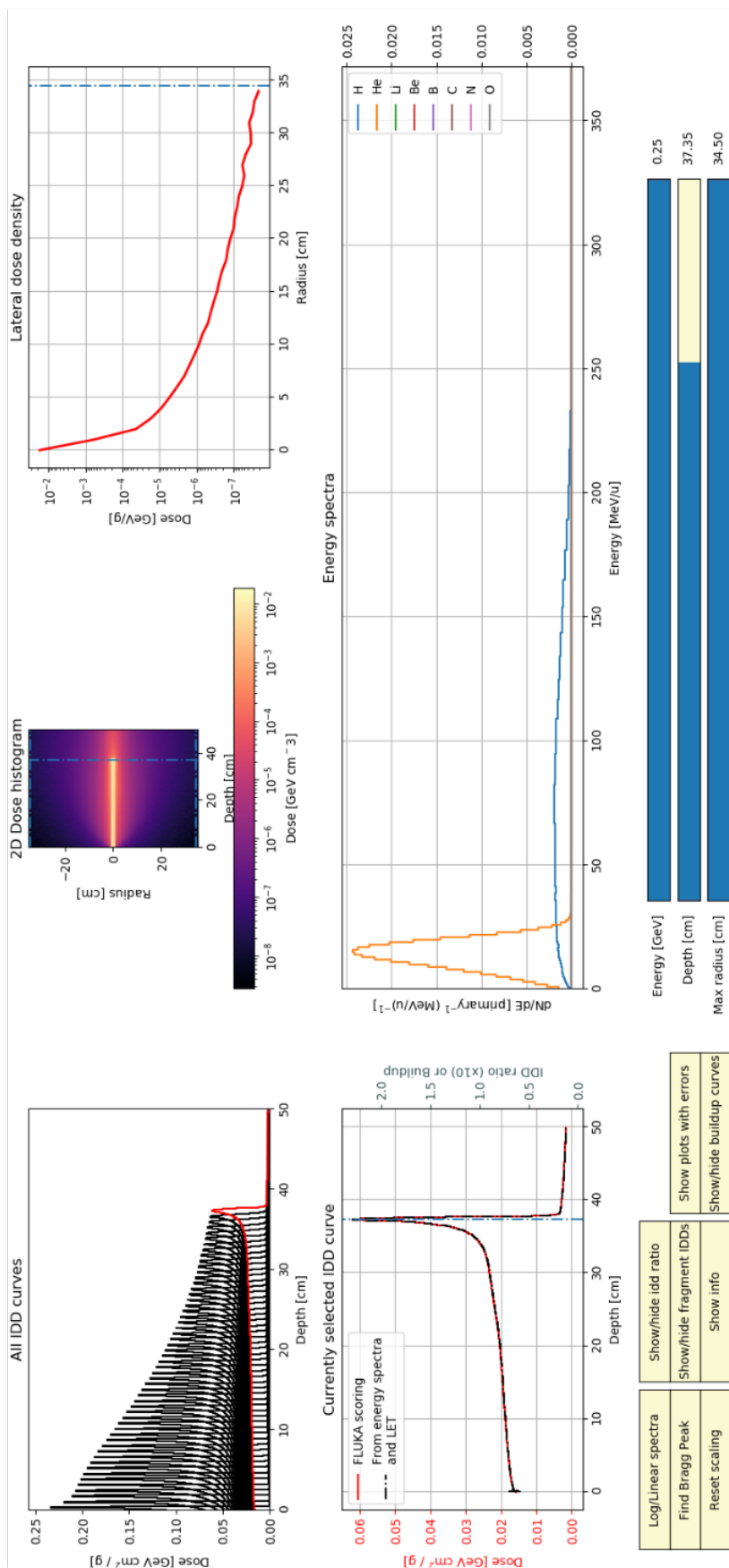
Figure B.1 displays the GUI, as described in section 3.2.3, deployed to show helium beams.

Fig. B.1 The GUI for helium beams.